March 18th, 2017

Complementary subnetworks of cortical somatostatin interneurons

Alexander Naka[1], Ben Shababo[1], Benjamin Snyder[2], Andrew Y. Egladyous[2], Savitha Sridharan[2], Liam Paninski[3,4,5,6], and Hillel Adesnik[1,2,7]

[1]Helen Wills Neuroscience Institute and [2]Department of Molecular and Cell Biology at the University of California, Berkeley; Berkeley, California, USA

Neurobiology and Behavior Program[3], Center for Theoretical Neuroscience[4], Departments of Statistics and Neuroscience[5], and Grossman Center for the Statistics of Mind[6] at Columbia University; New York City, New York, USA.

[7]Corresponding author

Abstract

The connectivity patterns of excitatory and inhibitory microcircuits are fundamental to computation in the neocortex. Highly specific excitatory projections form a stereotyped microcircuit linking the six cortical layers, but it is unclear whether inhibitory circuits are structured according to a similar layer-based logic or instead wire up non-selectively across the different layers. Understanding principles of inhibitory wiring is critical, since they constrain the computational operations that cortical inhibition can perform. If subnetworks of inhibitory neurons target specific functional components of cortical circuits (e.g. cortical input and output layers), these targets could be independently modulated, enabling a richer repertoire of inhibitory computations. Here we use one and two photon optogenetic circuit mapping techniques to demonstrate that two distinct subtypes of spatially intermingled Layer 5 (L5) somatostatin (SOM) interneurons form exquisitely selective and complementary intracortical circuits. One subtype connects predominantly with L4 and L6 - the primary cortical input layers, while a second subtype connects nearly exclusively with L2/3 and L5 - the primary cortical

output layers. This highly specific architecture suggests that separate SOM networks could differentially modulate processing at the input and output stages of the neocortical microcircuit.

Keywords: cerebral cortex; interneuron; somatostatin; neural circuit; inhibition; cortical layers; optogenetics; two photon; connectivity

Introduction

Excitatory and inhibitory synaptic connectivity are fundamental to computation in neural circuits. In sensory regions, such as the primary somatosensory cortex (S1), excitatory circuitry follows a modular architecture centered on the 6-layered structure of neocortex. Excitatory principal cells (PCs) in each layer differentially encode and process sensory information, and their inter-connectivity helps define the basic input/output logic of the S1 microcircuit (Feldmeyer, 2012; Harris and Shepherd, 2015). 'Bottom-up' sensory inputs enter S1 via thalamocortical projections that most densely innervate L4, and cortical output emerges primarily from PCs in L2/3 and L5, feeding forward to other brain regions. In between, sensory-driven activity propagates through the different layers via highly specific translaminar pathways. Together, these excitatory pathways comprise a stereotyped microcircuit, which is thought underlie hierarchical transformation and processing of sensory information (Atencio et al., 2009; Martinez et al., 2005).

In contrast, no comparable framework exists for inhibitory circuit organization. While it is well established that the connectivity of many inhibitory circuits is selective with respect to cell-type (especially interneuron-to-interneuron connectivity; Kepecs and Fishell, 2014; Pfeffer et al.,

2013), and that many interneurons target specific subcellular compartments of other neurons (Markram et al., 2004; Tremblay et al., 2016), it remains unclear how inhibitory circuits integrate into the layer-based logic of the excitatory microcircuit. One possibility is that interneurons non-selectively interconnect with PCs (Bock et al., 2011; Fino and Yuste, 2011; Hofer et al., 2011; Packer and Yuste, 2011; Scholl et al., 2015), irrespective of layers; this would suggest that cortical inhibition primarily performs 'global' operations on excitatory neurons, such as non-specific normalization (Carandini and Heeger, 2012; Poo and Isaacson, 2009; Pouille et al., 2009a). Alternatively, interneurons might form synaptic connections with specific layers within the microcircuit, which would suggest that different functional components of cortical circuits (e.g. cortical input and output layers) can be independently modulated by specific inhibitory pathways, enabling more sophisticated computations.

To resolve this, it is necessary to assess connectivity in inhibitory circuits with respect to both layer and cell-type, since different classes of interneurons likely obey different principles for translaminar wiring. For example, many interneurons, including parvalbumin (PV) cells, the most numerous class of cortical interneuron, are largely local, intralaminar inhibitors (Brill et al., 2016; Koelbl et al., 2015; Levy and Reyes, 2012; Packer and Yuste, 2011; but see Bortone et al., 2014; Buchanan et al., 2012). However, some types of interneurons - most notably, dendrite-targeting somatostatin (SOM) interneurons- appear specialized to mediate translaminar inhibition (DeNardo et al., 2015; Helmstaedter et al., 2009; Jiang et al., 2013, 2015; Kätzel et al., 2011; Marques-Smith et al., 2016; Wang et al., 2004; Xiang et al., 1998). SOM cells are critical players in many aspects of neural computation, perception, and cognition (Adesnik et al., 2012; Kim et al., 2016; Kvitsiani et al., 2013; Lee et al., 2012; Makino and Komiyama, 2015; Urban-

Ciecko and Barth, 2016). Since they integrate excitatory inputs from both intralaminar and translaminar sources and since many SOM cells, including L1-targeting Martinotti cells (MCs), project extensive translaminar axons they are likely key players in translaminar inhibitory circuitry (Apicella et al., 2012; Kapfer et al., 2007; Karnani et al., 2016; Otsuka and Kawaguchi, 2009; Silberberg and Markram, 2007; Xu and Callaway, 2009; Yoshimura and Callaway, 2005). How do SOM inhibitory networks integrate into the different layers of the cortical microcircuit?

The intralaminar outputs of SOM cells onto nearby PCs are thought to be extremely dense (Fino and Yuste, 2011; Jiang et al., 2015), which has led to the hypothesis that SOM cells might generate a 'blanket of inhibition' that overlays nearby excitatory circuits (Fino et al., 2013; Karnani et al., 2014). One possibility is that the translaminar connectivity of SOM cells is similarly non-selective. However, more sophisticated principles might govern the organization of laminar SOM circuits. SOM cells are highly heterogeneous (Urban-Ciecko and Barth, 2016; Yavorska and Wehr, 2016) and can be subdivided into electrophysiologically and genetically distinct subtypes (Tasic et al., 2016). Intriguingly, the axons of different SOM subtypes arborize in specific laminar domains (Ma et al., 2006; Muñoz et al., 2014, 2017), suggesting that different subtypes could potentially influence unique aspects of cortical processing by targeting specific components of the cortical microcircuit. Furthermore, emerging evidence indicates that SOM subtypes also exhibit distinct sensory tuning and coupling to behavior (Kim et al., 2016; Kvitsiani et al., 2013; Ma et al., 2010; Muñoz et al., 2017; Nakajima et al., 2014; Reimer et al., 2014). However, we lack even basic knowledge of the local input-output organization of SOM subtypes – a necessary prerequisite for reaching mechanistic explanations for how they might perform unique computations and influence specific cortical dynamics. What are the patterns of

synaptic input to different types of SOM cells, and how might these give rise to differential activation of SOM subtypes during sensation and behavior? Do all SOM cells generate non-selective inhibitory outputs, or can SOM cells provide targeted inhibition to specific components of the cortical microcircuit, such as certain cortical layers?

To address these issues, we used a combination of high-resolution one and two photon optogenetic mapping, paired intracellular recordings, and anatomical reconstructions to probe the logic of SOM inhibitory circuits across the six cortical layers. We focused on SOM cells in L5, the layer in which they are most abundant (Markram et al., 2004; Rudy et al., 2011) and found that two subtypes of SOM cells exhibit strikingly complementary laminar patterns of connectivity. L5 Martinotti cells receive input from L2/3 and L5, whereas L5 non-Martinotti cells receive input from L4 and L6. In turn, L5 Martinotti cells provide reciprocal inhibition to L5 PCs but not L4 PCs, while L5 non-Martinotti cells inhibit L4 PCs but not L5 PCs. These results demonstrate that subtypes of L5 SOM cells, while spatially intermingled, are wired into separate layer and cell-type specific subnetworks. Since L4 and L6 collectively represent the primary input zones of the cortex while L2/3 and L5 are the major feedforward output streams, this split architecture suggests that these SOM networks can independently inhibit different nodes in the cortical microcircuit and thereby flexibly modulate specific aspects of cortical computation.

Results

Distinct subtypes of L5 SOM cells receive complementary patterns of excitatory synaptic input

To probe the structure of L5 SOM circuits, we first sought to verify that we could identify and target different subtypes of SOM cells in acute slices from the barrel cortex. We employed three transgenic lines of mice: a double transgenic SOM-Cre x LSL-tdTomato line (hereafter SOM-TdT) in which nearly all SOM cells are labeled, the GIN line, which primarily labels L1-targeting Martinotti cells (MCs) with GFP, and the X94 line, which labels an alternative population of non-Martinotti cells with GFP (Ma et al., 2006; Oliva et al., 2000; Taniguchi et al., 2011). Biocytin fills confirmed that the vast majority of L5 GIN cells were MCs (41/44; 93%) which exhibited an ascending translaminar axon that ramified in L1, L2/3, and L5a (Fig. 1a) and intrinsic properties classically associated with MCs (Fig. S1; Fanselow et al., 2008; Kawaguchi, 1993; Kinnischtzke et al., 2012; Wang et al., 2004). Similarly, the vast majority of L5 X94 cells were non-Martinotti cells (32/35; 91%) which formed a dense axonal plexus in L4 rather than L1 (Fig. 1a, Fig. S2) and exhibited quasi-fast-spiking electrophysiological phenotypes (Fig. 1b, Fig. S1). While the X94 line labels only ~15% of SOM cells in L5 (Ma et al., 2006), additional recordings from L5 SOM-TdT cells suggested that a larger fraction (~30 - 40%; Fig. S1c-g) of L5 SOM cells are non-Martinotti, X94-like cells (hereafter termed 'XCs') with most of the remainder being MCs. Thus L5 contains at least two intermingled but qualitatively distinct SOM cell subtypes, MCs and XCs, which can reliably be identified using the GIN and X94 lines, respectively (Ma et al., 2006).

Aligning reconstructions of L5 MCs and XCs revealed that these two populations had strikingly complementary vertical profiles of neurite density: MCs primarily innervated layers 1, 2/3 and 5, and XCs primarily innervated L4 and the L5/L6 border (Fig. 1c). Since stereotyped neurite geometry is a key determinant of excitatory connectivity between different types of PCs

(Shepherd and Svoboda, 2005), the anatomical disparity between MCs and XCs suggested that subtypes of SOM cells might also preferentially send and/or receive translaminar synaptic connections with different layers. However, very little is known about whether or how MCs and XCs are differentially wired into the cortical circuit.

To address this possibility, we first asked whether the excitatory inputs to MCs and XCs might arise from different laminar sources. We virally expressed channelrhodopsin-2 (ChR2) in all excitatory neurons and photo-stimulated PCs in different regions of the slice to map the excitatory inputs to L5 MCs and XCs (Fig. 1d,e,f, AAV-flexed-ChR2 in the emx1-Cre line; see methods and Fig. S4). Remarkably, we found that L5MCs and XCs receive inputs from highly specific but largely non-overlapping sources that aligned with the anatomical distributions of their neurites. L5 MCs, but not L5 XCs, frequently received excitatory inputs from either upper L5, L2/3, or from both L2/3 and L5, but received little input from L4 or L6. On average, MCs received stronger inputs from L2/3 than L5 (49 ± 9% of total input from L2/3 versus 26 ± 7% from L5 in n = 15 MCs; p = 0.008, paired t-test). These results are consistent with previous studies (Anastasiades et al., 2016; Jiang et al., 2015; Kapfer et al., 2007; Pluta et al., 2015). In contrast, L5 XCs received strong input from L4 and/or the L5B/L6 border (Fig. 1e,f; input from L4 and L6 was 62 ± 7% of total input for n = 14 XCs versus 25 ± 3% for n = 15 MCs; $p = 6.5 \cdot 10^{-10}$; two sample T-test; see also Fig. S3) but relatively little input from L2/3 and L5. This input architecture indicates that these two subtypes of L5 SOM cells receive almost completely distinct patterns of excitatory innervation from their local circuit. Comparing the average laminar profiles of mapped excitatory input and anatomical reconstructions revealed a striking symmetry in the overall structure of XC and MC intracortical circuits: XCs received input from L4

and 6, and projected most densely to these two layers; MCs received input from L2/3 and 5, and projected preferentially to these same two layers (Fig. 1c,f).

The striking laminar differences in inputs to L5 XCs and MCs suggested that these two types of SOM cells should be differentially recruited by activity of different cortical layers. For instance, driving L4 should specifically recruit XCs, but not MCs. To test this possibility, we specifically photo-stimulated L4 excitatory neurons via Cre-dependent expression of ChR2 in scnn1-Cre mice (crossed to GIN or X94; Fig. 2a). L4-specific photostimulation (with two different stimulus protocols, across four different intensities; see methods) drove large EPSCs in XCs but evoked little to no input in MCs under identical conditions (Fig. 2b,c; Fig. S5). Current clamp recordings under the same conditions showed that L4 photo-stimulation reliably drove spiking in L5 XCs, but not in L5 MCs (Fig. 2b,d; Fig. S5), despite the fact that MCs are intrinsically more excitable than XCs (Fig. S1). The lack of evoked responses in MCs was not due to differences in the degree of L4 activation (see supplemental text and Fig. S5 for controls). Thus, these results indicate a stark difference between L5 XCs and MCs: L4 densely innervates and powerfully drives firing in L5 XCs, but not L5 MCs.

Common input mapping reveals subnetwork structure in L5 SOM cell output

Having found that XCs and MCs in L5 receive highly complementary patterns of excitatory synaptic input, we next asked whether XCs and MCs also exhibit layer-specificity in their inhibitory outputs. Since SOM cells have been implicated in generating feedback inhibition (Adesnik et al., 2012; Kapfer et al., 2007; Silberberg and Markram, 2007), we hypothesized that MCs and XCs might target their inhibitory outputs in order to reciprocally inhibit the same PC

populations that excite them. For example, XCs but not MCs would inhibit L4 PCs, whereas MCs but not XCs inhibit L5 PCs. Alternatively, MCs, XCs, or both cell types could globally target PCs within and across layers non-selectively. These hypotheses are difficult to test using conventional optogenetic approaches since, to our knowledge, Cre-driver lines do not exist for all SOM subtypes. This precludes specific photo-stimulation of MCs or XCs *en masse*. An alternative approach is to use high precision photo-stimulation to ask whether the outputs of individual SOM cells (in the non-specific SOM-Cre line) diverge onto PCs in multiple layers. If individual SOM cells target either L4 or L5 PCs, but not both, then we should never observe common input to pairs of L4 and L5 PCs when photo-stimulating single SOM neurons. This can be tested by mapping SOM inhibitory connections onto multiple PCs simultaneously and analyzing the spatiotemporal coincidence of evoked IPSCs onto different pairs of PCs, thereby measuring the amount of common input shared between pairs of PCs in different layers (Morgenstern et al., 2016; Yoshimura et al., 2005). Although this approach does not discriminate between MCs and XCs directly, it performs a more stringent test by extending our hypothesis to apply to the structure of the outputs of the L5 SOM population as a whole.

In order to conduct comprehensive mapping of individual SOM outputs, we developed a novel approach to map neural circuits at high spatiotemporal resolution using two photon optogenetics and a statistical pipeline for detecting synaptic connections (Merel et al., 2016) and evoked inhibitory postsynaptic current (IPSC) synchrony. In addition, we employed a soma-targeted opsin (Wu et al., 2013), which has the advantage of providing far superior spatial resolution during photo-stimulation than non-targeted opsins (Fig. 3a,b,c; Baker et al., 2016). We expressed a soma-targeted variant of the red-shifted opsin, ChrimsonR, in SOM cells using

the SOM-Cre line, and photo-stimulated SOM cells using 2-photon excitation with computer generated holography (Fig. 3a,b; Fig. S9a). Since SOM → PC synapses are often located on the distal dendrites of PCs, we recorded IPSCs using a cesium-based internal solution and took additional steps to minimize false negatives (see Methods). Using this method, we simultaneously mapped SOM inputs to pairs of L4-L5 PCs and L5-L5 PCs (Fig. 3d,e,f). We found that L5 PCs received SOM inputs at more locations than L4 PCs on average (45.3 ± 5.5 inputs out of 441 locations tested per map in n = 30 L5 PC maps versus 12.8 ± 2.3 inputs in n = 10 L4 PC maps, Fig. S10e), but that both cell types received inputs from locations throughout L5 (Fig. S10f).

If individual L5 SOM cells target either L4 PCs or L5 PCs but not both, we would expect maps from L4-L5 PC pairs to contain spatially intermixed but non-overlapping input locations. Conversely, when recording a pair of L5 PCs, we would expect a much higher rate of overlap due to common input from MCs. Consistent with this hypothesis, we observe that the probability of detecting an input at the same location in L4-L5 pairs was very low and substantially smaller than for L5-L5 pairs (2.4 ± 1.3% spatially coincident inputs out of all input locations in n = 10 L4-L5 pairs, versus 28 ± 6.7% in n = 10 L5-L5 pairs; $p = 1.2 \cdot 10^{-3}$, Wilcoxon rank sum test). Given that occasionally more than one SOM cell might be photostimulated at any given location (Fig. S9d,g), we employed a statistical test for fine time scale synchrony of IPSCs between the patched cells at each candidate location (where both cells received input) to determine whether the IPSCs truly arose from a single SOM cell diverging onto both recorded PCs (Amarasingham et al., 2012, see Methods, Fig. 3g, Fig. S10g,h,i,j). Using this far more stringent spatiotemporal test for the detection of common input, we detected no locations in

which stimulation evoked common inputs for L4-L5 pairs, whereas we detected at least one common input in 7 of 10 L5-L5 pairs (Fig 3h; no locations in n = 10 L4-L5 pairs versus 13.7 ± 5.1% of all input locations in n = 10 L5-L5 pairs; $p = 1.1 \cdot 10^{-3}$, Wilcoxon rank sum test; see also Fig. S10k). These data argue that individual L5 SOM cells connect to either L4 PCs or to L5 PCs, but never to both. In other words, L4 PCs and L5 PCs are inhibited by non-overlapping subnetworks of L5 SOM cells.

Paired recordings show dense, reciprocal, and selective intra- and translaminar connectivity

We hypothesized that the L4-targeting and L5-targeting populations of L5 SOM cells identified with two-photon optogenetic mapping corresponded to XCs and MCs. This would mean that SOM cells in L5 are organized into at least two discrete subnetworks, each with its own unique input and output connectivity. If this were the case, one would expect L5 XCs to be reciprocally connected with L4 PCs, but not L5 PCs; conversely, L5 MCs should be reciprocally connected with L5 PCs but not L4 PCs. To address this, we conducted a large set of paired intracellular recordings to assess the fine-scale patterns of synaptic connectivity between L4/L5 PCs and L5 MCs/XCs. This strategy is low throughput, but provides unambiguous measurements of synaptic connectivity between identified cell types; furthermore, it complements the above experiments because it is unaffected by issues that potentially limit optogenetic approaches (for example, differences in intrinsic excitability between cell types or variability in opsin expression). In addition to targeting L5 MCs and XCs with the GIN and X94 lines as above, we also used the SOM-TdT line to identified L5 SOM cells, which we classified as putative MCs or XCs based on their electrophysiological properties (Fig. S1g; Table S1).

First, we address translaminar connections. Paired recordings between L5 XCs and L4 PCs revealed monosynaptic L5 XC→ L4 PC connections, which we observed as short-latency IPSP/IPSCs in the L4 PC membrane potential following induced action potentials in the L5 XC. We observed frequent L5XC→L4PC connections (36/67 pairs tested; 54%; Fig. 4a,b), even across relatively long inter-somatic distances (183 ± 67 µm, mean ± S.D.; Fig. S6), suggesting that L5 XCs connect densely onto L4. We also frequently observed monosynaptic excitatory connections from L4 PCs onto L5 XCs, consistent with the optogenetic experiments above (39/72 pairs tested; 54%). These synapses exhibited profound facilitation during sustained high-frequency firing in the presynaptic cell (Fig. 4a; Fig. S8), the hallmark of excitatory connections onto SOM cells (Beierlein et al., 2003; Berger et al., 2009; Kapfer et al., 2007). In cases where we tested connectivity bidirectionally, we frequently observed reciprocal connections (23/56 pairs tested; 41%). Thus, L5 XCs and L4 PCs form a translaminar feedback inhibitory motif. We also observed frequent connections from L5 XCs onto L4 fast-spiking (FS) cells (12/23 pairs tested; 52%; Fig. S7), consistent with a known circuit in which L4 non-Martinotti SOM cells inhibit L4 FS cells (Ma et al., 2006; Xu et al., 2013).

In contrast, we very rarely observed excitatory connections from L4 PCs to L5 MCs (1/95 pairs tested; 1%; Fig. 4a,b) or from L5 MCs onto L4 PCs (4/68 pairs tested; 6%), despite the fact that these pairs were separated by smaller inter-somatic distances than L4PC-L5XC pairs (143 ± 47 µm, mean ± S.D.; Fig. S6), likely due to the fact that MCs and XCs preferentially localize in the superficial and deeper portions of L5 respectively (Ma et al., 2006). In a subset of these experiments, we recorded from L4 PCs in the voltage clamp configuration at +10mV (using a cesium-based internal solution), but did not observe connections any more frequently (0/38

pairs tested; 0%). These data suggest that L5 XCs are integrated into the densely interconnected network of L4 PCs and interneurons (Beierlein et al., 2000; Petersen and Sakmann, 2000), whereas L5 MCs are essentially isolated from it. Since our 2P mapping experiments indicated that distinct sets of SOM cells inhibit L4 PCs and L5 PCs, we hypothesized that this pattern would be reversed within L5, i.e. L5 MCs but not L5 XCs will interconnect with L5 PCs.

We next examined intralaminar connections between L5 PCs and L5 SOM cells. We observed frequent inhibitory connections from L5 MCs onto L5 PCs (24/46 pairs tested; 52%; Fig. 4c,d), in agreement with a large body of work indicating that Martinotti cells diverge profusely onto nearby intralaminar targets (Berger et al., 2010; Fino and Yuste, 2011; Jiang et al., 2015). We also observed excitatory connections from L5 PCs onto L5 MCs, albeit more rarely (4/29 pairs tested; 14%; Fig. 4c,d) but at a rate consistent with the literature (Jiang et al., 2015; Levy and Reyes, 2012). In contrast, we detected very few inhibitory outputs from L5 XCs onto L5 PCs (2/65 pairs tested; 3%; Fig. 4c,d) or excitatory connections from L5 PCs onto L5 XCs (1/60 pairs tested; 2%; Fig. 3c,d), despite the fact that L5 PCs were on average located much closer to L5 XCs than were L4 PCs. The surprising dearth of intralaminar connectivity between L5 PCs and L5 XCs stands in stark contrast to the dense intralaminar connectivity observed between L5 PCs and L5 MCs, as well as in other inhibitory circuits (Fino and Yuste, 2011; Levy and Reyes, 2012; Packer and Yuste, 2011), lending further support to the notion that MC and XC circuits are uniquely and selectively wired (Fig. 4e).

Discussion

Understanding of the organization of cortical inhibitory circuits has surged in recent years, but the integration of these new architectures with the established, layer-centric framework of the excitatory cortical microcircuit has proved elusive. Our data establish previously unknown excitatory-to-inhibitory and inhibitory-to-excitatory pathways involving two subnetworks of L5 SOM interneurons, which are both layer and cell-type specific. Optogenetic circuit mapping shows that L5 MCs receive excitatory inputs chiefly from PCs in L2/3 and L5, the primary cortical output layers, while L5 XCs receive inputs mainly from PCs in L4 and upper L6, the primary input zones for afferent input from the ventral posteromedial thalamus (Wimmer et al., 2010). Paired recordings and 2-photon holographic optogenetic interrogation of common SOM-mediated input indicate that in turn, these same SOM subtypes selectively inhibit the same PC populations that excite them, at least within L4 and L5. Thus XCs and MCs, though spatially intermingled in L5, are functionally segregated into two disjoint networks with selective and complementary laminar connectivity (Fig. 4e).

Dense but selective inhibitory wiring

These results reveal a previously unknown, striking degree of specificity in the inhibitory cortical wiring diagram. In particular, the observation that L5 XCs exhibit nearly no intralaminar connectivity with L5 PCs, but do engage in dense, reciprocal connectivity with L4 PCs is inconsistent with the idea of a single, global blanket of SOM-mediated inhibition. Instead, SOM-PC circuits appear to more closely resemble a patchwork quilt, comprised of multiple networks of SOM subtypes which independently service separate spatial domains. SOM-PC connectivity can be extremely dense and non-selective within one of these domains (e.g. creating a blanket

within a single laminar microcircuit), but highly selective on the scale of layers and columns. Though we did not investigate it in this study, it seems likely that selective connectivity on this scale could be achieved, at least in part, simply by SOM subtypes having preferred laminar targets for axonal arborization (Packer et al., 2012).

Functional implications of separate, layer-specific SOM feedback circuits

The circuit structure established here suggests that at least two different pools of SOM-mediated inhibition separately modulate successive stages of cortical processing. XCs will chiefly be recruited as a function of the 'input' of the microcircuit, generating inhibition proportional to the amount of activity in the input layers and thalamus, which in turn varies widely depending on external sensory drive. Conversely, MCs will be recruited by activity in L2/3 and L5 PCs, whose projections represent the major feedforward pathways out of S1 (Harris and Shepherd, 2015); consequently, MCs will generate feedback inhibition as a function of the 'output' of the microcircuit. This raises the possibility that MC and XC-mediated feedback inhibition could differentially contribute to various forms of population gain control: XCs could perform input-scaling on the gain, whereas MCs could regulate output-scaling. These different modes of gain control have been proposed to perform myriad functions in perception and cognition (Carandini and Heeger, 2012; Miller, 2016; Salinas and Thier, 2000), and the circuit mechanisms of gain modulation are a topic of intense recent focus (Atallah et al., 2012; Fu et al., 2014; Lee et al., 2012; Litwin-Kumar et al., 2016; Pakan et al., 2016; Pouille et al., 2009b; Seybold et al., 2015; Wilson et al., 2012). Independent modulation of different SOM circuits, either by the intracortical excitatory circuits described here, long range inputs from thalamus or

higher cortical areas, or by other sources such as VIP-mediated inhibition (Lee et al., 2013; Muñoz et al., 2017; Pfeffer et al., 2013; Pi et al., 2013) or neuromodulation (Polack and Contreras, 2012; Xiang et al., 1998; Xu et al., 2013) could represent a mechanism by which the brain dynamically fine-tunes the cortical population input-output function.

Furthermore, these parallel subnetworks of SOM inhibition might also fine-tune how the sensory cortex integrates 'bottom-up' and 'top-down' inputs, as bottom-up is conveyed via thalamocortical axons primarily (though not exclusively; Constantinople and Bruno, 2013) to L4, and thus is most directly affected by XC-mediated inhibition, while top-down inputs are thought to be conveyed to the apical dendrites of L5 and L2/3, and thus are primarily modulated by MC-mediated inhibition (Murayama et al., 2009; Petreanu et al., 2012). Therefore, the parallel structure of MC and XC networks could allow S1 to independently alter its sensitivity to top-down and bottom-up input streams to optimize the behavioral responses to sensory stimuli. Supporting this proposal, recent studies have observed that subtypes of SOM cells with either wide or narrow spike waveforms (which might correspond to MCs and XCs) are differentially activated during various behavioral contingencies (Kim et al., 2016; Kvitsiani et al., 2013; Muñoz et al., 2017; Reimer et al., 2014). Pressing questions for future investigation will be to determine how excitatory drive from different laminar PC populations contributes to the unique activity patterns of SOM subtypes, and conversely, to determine how distinct SOM subtypes differentially shape the dynamics of the cortical microcircuit. Future experiments could address these questions by optogenetically manipulating specific SOM subtypes using intersectional genetics (He et al., 2016) or with a Cre-DOG based approach (Tang et al., 2015). Nearly all optogenetic manipulations of SOM cells have employed the non-specific

SOM-Cre line, which could explain the somewhat heterogeneous results that have emerged, including both inhibition and disinhibition (Cottam et al., 2013; Lee et al., 2012; Seybold et al., 2015; Wilson et al., 2012; Xu et al., 2013). More precise manipulations of SOM subtypes (e.g., MCs vs. XCs) could help reveal the functional impacts of distinct SOM subnetworks.

The selective inhibitory 'pathways' described here also suggest specific predictions about how different SOM subtypes shape the dynamics of cortical activity. For example, within layers, XCs and MCs will respectively mediate L4→L4 and L5→L5 feedback dendritic inhibition (Silberberg and Markram, 2007). Across layers, SOM cells should contribute to L2/3→L5 feedforward inhibition (Adesnik and Scanziani, 2010; Apicella et al., 2012; Pouille et al., 2009a), but not to L4→L5 translaminar inhibition, implying that the latter operates solely through parvalbumin-expressing FS interneurons (Pluta et al., 2015). Furthermore, XCs (but not MCs) receive strong thalamocortical input (Hu and Agmon, 2016; Ji et al., 2016; Tan et al., 2008) and are thought to generate feedforward inhibition in response to sustained thalamic activity; our data therefore imply that SOM-mediated thalamocortical feedforward inhibition will impinge upon L4 neurons but not L5 PCs.

Diversity of L5 SOM cells

We find that XCs comprise a large fraction of L5 SOM cells and perhaps of SOM cells more generally (see Fig. S1g and supplemental text). If XCs are so prevalent, one might ask why they have been reported on only sparingly. Beyond studies which used the X94 line (Hu and Agmon, 2016; Ma et al., 2006; Tan et al., 2008), close examination of the literature reveals several reports of cells with L4-targeting morphologies and other properties characteristic of XCs

(Fairén et al., 1986; Helmstaedter et al., 2009; Kumar and Ohana, 2008; Porter et al., 2001), which have sometimes been called 'Lorente de Nó cells' in attribution to their earliest describer (Cobas et al., 1987; Fairén, 2007; Lorente de No, 1992). The previous lack of genetic tools to target these cells may have hindered detailed investigation of XCs until now; however, L5 XCs bear striking resemblances to non-Martinotti SOM cells in L4 (see Fig. S4 and supplemental text) which are well studied by comparison (Beierlein et al., 2000, 2003; Ma et al., 2012; Xu et al., 2013). It is also likely that XCs have sometimes been misclassified as fast-spiking cells due to their quasi-fast-spiking intrinsic properties, especially in studies done without genetic or immunohistochemical markers for somatostatin and parvalbumin. This issue likely also applies to studies performing *in vivo* extracellular recordings, since spike waveforms of XCs are similar to those of true parvalbumin-expressing FS cells (Kim et al., 2016; Kvitsiani et al., 2013; Muñoz et al., 2014).

Although our data clearly delineate two very distinct subtypes of SOM cells in L5 and their intracortical circuits, an important limitation of this study is the need to use the GIN and X94 lines to target MCs and XCs. SOM cells are highly heterogeneous, even within the subsets labeled by these lines (particularly the GIN line; Halabisky et al., 2006; McGarry et al., 2010) and other subtypes of SOM cells not covered by these lines are known to exist, including long-range projecting SOM cells that are most prevalent in L6 (He et al., 2016; Ma et al., 2006; Tasic et al., 2016; Yavorska and Wehr, 2016). It is likely that other subtypes also exhibit specific connectivity schemes which may be different from the ones described here. Most notably, L5 also contains at least one other type of 'T-shaped' MC which is labeled by the X98-GFP and the Chrna2-Cre transgenic lines (Hilscher et al., 2016; Ma et al., 2006). T-shaped MCs are morphologically and

electrophysiologically distinct from the L5 MCs labeled by the GIN line. Unlike L5 GIN MCs, which inhibit both thick and slender-tufted L5 PCs (data not shown), T-shaped MCs specifically inhibit thick-tufted but not slender-tufted L5 PCs and have been implicated in mediating frequency-dependent disynaptic inhibition between these neurons (Berger et al., 2010; Hilscher et al., 2016; Silberberg and Markram, 2007). Since we observed relatively little intralaminar excitatory input onto L5 GIN MCs, one possibility is that T-shaped MCs also possess their own unique circuit scheme, with relatively stronger intralaminar connectivity. Future work is needed to determine how closely laminar connectivity is tied to the cellular identity of other SOM subtypes (and of cortical interneurons more generally) and whether this connectivity changes during development (Anastasiades et al., 2016; Marques-Smith et al., 2016; Tuncdemir et al., 2016) and learning (Kato et al., 2015; Kätzel and Miesenböck, 2014; Makino and Komiyama, 2015). Taken together, the data in this study establish two new fundamental inhibitory motifs in the cortex: two subnetworks of SOM cells target specific cortical compartments – the input and output cortical layers, potentially providing a means to fine tune cortical computation during different sensory or behavioral demands.

Methods

All experiments were performed in accordance with the guidelines and regulations of the Animal Care and Use Committee of the University of California, Berkeley.

Transgenic mice

The following mouse lines were used for this study: the scnn1-tg3-Cre line (JAX stock # 009613), the emx1-IRES-Cre line (JAX stock #005628), the PV-IRES-cre line (B6;129P2-

Pvalbtm1(cre)Arbr/J ; JAX stock #008069), the SOM-IRES-cre line (JAX stock 013044), the GIN line (FVB-Tg(GadGFP)45704Swn/J; JAX stock #003718), the X94-GFP line (Tg(Gad1-EGFP)94Agmo/J; JAX stock 006334), the Ai9 Rosa-LSL-tdTomato line (JAX stock # 007909). Mice were housed in cohorts of five or fewer with a light:dark cycle of 12:12 hours, and were used for experimentation during their subjective night.

Viral Infection

Neonatal mice (p0-3) were deeply cryo-anesthetized and placed in a head mold. Viral aliquots were loaded into a Drummond Nanoject injector and injected into 4 sites in the barrel cortex of the left hemisphere. At each site, virus was injected at multiple depths (2 depths for scnn1-tg3-cre and drd3-cre mice, 3 depths for emx1-IRES-Cre and SOM-IRES-cre mice) in increments of 18.4 nL or 36.8 nL (for multiphoton experiments), for a total of ~150-440 nL of virus injected per mouse. Following injections, mice were moved to an incubation chamber for recovery, and were returned to the dam once they regained color and began to move. Viruses used were AAV9-CAG-flexed-Chr2-tdTomato (acquired from the University of Pennsylvania Vector Core; undiluted for scnn1-tg3-cre and drd3-cre mice, diluted 1:1 with PBS for emx1-IRES-Cre mice), and AAV9-2YF-hSyn-DIO-ChrimsonR-mRuby2-Kv2.1.

Brain slice recording

Acute thalamocortical slices were prepared from mice (ages p14-29, at least 14 days after viral injection) as previously described (Adesnik and Scanziani, 2010b). Slices were placed in a recording chamber and constantly perfused with oxygenated artificial cerebro-spinal fluid (NaCl 119 mM, KCl 2.5 mM, $MgSO_4$ 1.3 mM, NaH_2PO_4 1.3 mM, glucose 20 mM, $NaHCO_3$ 26 mM,

$CaCl_2$ 2.5 mM) maintained at 32° C (21° C for multiphoton mapping experiments). Slices were oriented with the caudal surface facing up in the recording chamber. To ensure minimal disruption of vertical connectivity, all slices used for recording were inspected under infrared illumination at 40x magnification and/or post-hoc confocal imaging to confirm that pyramidal cell apical dendrites stayed roughly parallel with the surface of the slice or receded slightly deeper as they progressed apically. Whole cell recordings were performed using glass micropipettes (2-5MΩ resistance) pulled on a Sutter P-1000 Micropipette Puller. Pipettes were filled with a Cs^+ based internal ($CsMeSO_4$ 135 mM, NaCl 8 mM, HEPES 10 mM, Na_3GTP 0.3 mM, MgATP 4 mM, EGTA 0.3 mM, QX-314-Cl 5 mM, TEA-Cl 5mM) or a potassium gluconate based internal (K-gluconate 135 mM, NaCl 8 mM, HEPES 10 mM, Na_3GTP 0.3 mM, MgATP 4 mM, EGTA 0.3 mM). In some experiments, biocytin (0.4-1%) was dissolved into the internal solution to enable morphological recovery. Voltage recordings were not corrected for the junction potential. Series resistance was monitored with negative voltage steps during each trial, and was compensated up to 60%. Data were analyzed from recordings in which series resistance remained stable and below 30MΩ. Data were acquired and filtered at 2.2 kHz using a Multiclamp 700B Amplifier (Axon Instruments) and digitized at 20 kHz (National Instruments). All data were acquired using custom written MATLAB (Mathworks) software.

Characterization of intrinsic properties

In all recordings using K-based internal solution, an F-I curve was measured at the start of the experiment using a series of 1-second current injections, at -200 pA, -100 pA, and then proceeding in 50 pA increments from +50 to +500 pA. In some experiments, additional current

steps were manually designated and performed online to aid in estimation of rheobase. Resting membrane potential was defined as the median membrane potential during a baseline period measured immediately after break-in. Input resistance was calculated with Ohm's law using the steady state membrane potential during subthreshold current injections steps (current clamp) and/or the steady state current during 5 mV voltage steps (voltage clamp). Action potential onset was detected using code adapted from the Berg lab's *Spike_threshold_*PS function, which defines onset as the point of maximum positive slope in the phase space of the membrane potential and its first derivative (Sekerli et al., 2004). Spike width was measured as the full-width of each spike at the voltage halfway between the action potential threshold and the peak amplitude (half-max). Rheobase was estimated using the average of 1) a linear fit (with coefficients constrained to be nonnegative using the *lsqnonneg* function in MATLAB) of the F-I relation during the last subthreshold current injection step and the first few suprathreshold steps and 2) linear extrapolation of the current necessary to reach threshold based on measurements of the resting membrane potential, input resistance, and average threshold value of the first action potentials evoked during suprathreshold injections. These two measures were usually in good agreement. Adaptation index was calculated (following the Allen Brain Institute's Cell Types Database protocol) for each current injection using the expression:

$$\frac{1}{N-1}\sum_{n=1}^{N-1}\frac{ISI_{n+1}-ISI_n}{ISI_{n+1}+ISI_n}$$

Where N is the number of spikes during that current step and ISI is the interspike interval.

Paired recording connectivity testing

We first targeted whole-cell recordings to a fluorescent (GFP+ or TdTomato+) SOM cell, and then subsequently patched nearby neurons in the same slice. In some cases, we recorded serially from several neurons while maintaining the recording of the first neuron, in order to test multiple connections. Monosynaptic excitatory connectivity onto SOM cells was tested by driving trains of 10 spikes in the presynaptic cell at 70 Hz via current injection, while monitoring for EPSCs in the postsynaptic cell. Stimulation was repeated at least 15 times in all pairs tested. Monosynaptic inhibitory connectivity from SOM cells onto other neurons was tested by driving spikes in the presynaptic cell while monitoring postsynaptically for IPSCs (Cs-based internal, postsynaptic cell held at +10mV) or IPSPs (K-based internal, postsynaptic cell depolarized to approximately -52mV). Electrical connectivity between SOM cells was tested by hyperpolarizing each cell with 1-second current injections (at least 15 trials) while monitoring for hyperpolarization in the other cell.

For L5SOM-L5PC pairs, we recorded from both pyramidal tract and intratelencephalic type PCs, which could be distinguished by their laminar positions (preferentially L5B versus L5A), morphology visualized via infrared (large soma versus smaller soma) and post-hoc confocal imaging (thick-tufted apical dendrites versus slender-tufted), and/or their intrinsic properties (initial burst/doublet spiking followed by non-adapting spikes versus continuously adapting regular-spiking phenotype; Hattox and Nelson, 2007; Kim et al., 2015; Schubert et al., 2001). We did not observe any significant differences in the connectivity of either L5PC type with

L5MCs or XCs. For L5SOM-L4PC pairs, we did not distinguish between spiny stellate and pyramidal/star-pyramidal excitatory cells.

For paired recordings between L5 SOM cells and L4 FS/PV cells, we identified FS/PV cells using PV-Cre; LSL-TdTomato mice in some experiments (Fig. S7i). However, it was often difficult to visualize X94 cells using these animals due to the TdTomato fluorescence being much brighter than the GFP fluorescence. In other experiments (Fig. S7h), we targeted FS/PV cells in L4 by looking for L4 neurons with large cell bodies under IR, and then confirmed the identity of these cells electrophysiologically, with the primary criteria separating them from being narrow spike widths (slightly shorter than the average XC spike) and little or no spike frequency accommodation during high amplitude steps of current injection.

To classify SOM-TdT cells as putative XCs or MCs, we fit a support vector machine (cross validated 10-fold) to perform binary classification of L5 GIN cells and L5 X94 cells using only their intrinsic electrophysiological properties. We found that a classifier based on only two measures (spike width and estimated rheobase) performed just as well as multivariate classification based on a large number of metrics (~85% accuracy).We then used this classifier to predict the identity of a different dataset of L5 SOM cells recorded in SOM-TdT mice. This approach is likely to have resulted in a small number of SOM-TdT cells being misclassified; however, the connectivity of putative XCs and MCs were highly similar to the connectivity of XCs and MCs identified using the X94 and GIN lines. Furthermore, our conclusions about the differences in connectivity rates of L5 MCs and XCs with L4 and L5 PCs are unchanged by the exclusion of the SOM-TdT dataset, with the exception of L5PC→L5SOM connections – a circuit

which has been studied in some detail by others. This approach also effectively assumes a dichotomy in L5 SOM cells, since we have only two labels (MC and XC) to provide as training data, which is an important caveat since it is likely that further subdivisions of SOM cells exist in L5 (Ma et al., 2006). In a handful of cases, we recorded from SOM-TdT cells which appeared to be FS cells (Hu et al., 2013), with very narrow spikes, low input resistances, and a near complete lack of spike-frequency accommodation during high amplitude current injection steps; these neurons were excluded from further analysis.

Using paired recordings, we tested 544 total possible connections between 146 L5 SOM cells (39 L5 GIN cells, 53 L5 X94 cells, 54 L5 SOM-TdT cells) and PCs/FS cells in L4 and L5. Data from a subset of these neurons (n = 17 L5 GIN cells) were included in a previous study (Pluta et al., 2015). This dataset was unbalanced, and because in some cases we tested multiple connections onto the same L5 SOM cell, included some non-independent observations. Because of this, we used Monte Carlo permutation tests to test for significant differences between the connectivity rates of MCs and XCs. We generated a permuted dataset with the same observation structure (same number of L5 SOM cells and same number of connections tested per L5 SOM cell) in place for MCs and XCs by randomly resampling with replacement at both levels. We then measured the difference in observed connectivity rate for the MC and XC groups, and repeated this procedure 100,000 times to generate a null distribution of rate differences. We used this distribution to perform a 1-tailed test for significant differences between MC and XC connectivity rates for each type of connection tested (Table S1).

Optogenetic connectivity mapping *in vitro*

Experiments were done in slices from Emx1-Cre; GIN or Emx1-Cre; X94 mice injected with an AAV driving Cre-dependent expression of ChR2 in all excitatory cells. Whole cell voltage clamp recordings were performed in GFP+ L5 cells to target L5 MCs (Emx1-Cre; GIN) or L5 XCs (Emx1-Cre; X94). A digital micromirror device was used to focally photo-stimulate excitatory cells in different regions of the slice in order to map the spatial profile of excitatory inputs to recorded MCs and XCs.

Prior to experiments, slices were briefly visually inspected with epifluorescence under a 5x objective to confirm that a wide area containing dense, even expression of fluorescence (tagged to an opsin) was present in the barrel cortex. Recordings were targeted to within this region, which typically covered the entire lateral extent of barrel cortex in 4-5 slices. Slices in which expression appeared faint or uneven were discarded.

In some experiments, it was necessary to locate fluorophore-positive cells in slices also containing an excitatory opsin. To avoid excitotoxicity that can result from excessive illumination of opsin-containing neurons, we limited illumination to very brief intervals (1-2 seconds) while searching for fluorophore-positive cells. In some cases where the target cells were weakly fluorescent (young GIN and X94 animals), we searched for these cells while keeping the slice submerged in sucrose-substituted ACSF. Once target cells were located, this solution was washed out and replaced with normal recording ACSF prior to patching these cells and starting experiments.

DMD-based excitatory input mapping

Laser light was generated using a 1W 445nm diode laser (Ultralasers) and routed via a liquid light guide into a CEL5500 digital micromirror device (DMD) (Digital Light Innovations). The projection from the DMD was then collimated and integrated into the light path of the microscope, before being focused onto the slice chamber using a 5x (Olympus). For experiments using widefield illumination, the DMD passively reflected but not spatially modulate light. Prior to photo-stimulation, infrared and epifluorescence images were captured using an IR-1000 CCD camera (DAGE-MTI) and imported into MATLAB.

Excitatory mapping experiments were performed using a modified version of a previously described protocol (Pluta et al., 2015). Mapping was performed over an area extending from pia to the white matter, covering 2-4 barrel columns laterally (~400 to ~800 µm). For mapping excitatory inputs to GIN and X94 cells, the DMD was used to pattern light into a square region (75 µm x 75 µm). Each stimulation site was spaced 40µm apart from adjacent ones, resulting in some overlap of adjacent stimuli. We chose to 'ramp' our photostimulation, starting each stimulus with the light off and linearly increasing the light intensity over time. Ramping in this manner minimizes activation of fibers of passage (Adesnik and Scanziani, 2010). In each trial, a 'sawtooth' light stimulus composed of three successive 25ms ramps of light (1.25 mW/mm^2 final intensity) was applied to one stimulus site. This protocol was chosen in order to maximize the short-term facilitation of excitatory inputs to L5 SOM cells, though in practice we found it was usually possible to observe responses during the first ramp alone. Ten regions were stimulated per second in a serial, pseudorandom order, with 4 second breaks after every 10 seconds of mapping. Control experiments were performed using identical stimulation conditions while recording from $ChR2^+$ neurons in all layers. These experiments determined the

spatial resolution of photostimulation and confirmed that spiking was elicited in ChR2+ neurons only when regions very close to the soma were stimulated. We also included n = 2 experiments mapping inputs to L5 X94 cells which were performed using the exact mapping protocol described in (Pluta et al., 2015), though our results and conclusions were not substantially altered by their exclusion.

All data were analyzed using custom written MATLAB software. Data preprocessing consisted of removing baseline offsets and slow fluctuations from recordings by subtracting a down-sampled and median-filtered versions. Charge was calculated as the integral of the preprocessed recordings during photo-stimulation and the subsequent 25 milliseconds. To aggregate maps across cells, we first rotated the average map collected in each experiment in order to horizontally orient the laminar boundaries of the mapped area. Maps were next translated vertically to align the L4-L5 laminar boundary, and translated horizontally to align either the home column or the soma position of the recorded cell, before being horizontally cropped to an area ±300µm of their center and then averaged to yield a summary map.

For L4 stimulation experiments, we used widefield photostimulation through a 5x objective. We used two stimulation protocols: prolonged, 1-second ramps of linearly increasing light intensity and trains of ten pulses (1ms duration) at 40 Hz. We stimulated at 4 different intensities for each protocol. Since we sometimes recorded multiple neurons in the same slice (see Fig. S5), we fit generalized linear mixed effects models to the dose-response function of light-intensity versus evoked response (EPSC charge transfer or number of spikes), with fixed effects coefficients for the slope of this function for each cell-type and random effects slope

coefficients for each slice and neuron in the dataset as well as a constant intercept term. F-tests were used to test for differences in fixed effects coefficients. For paired analysis of L4 XCs and L5 MCs/XCs (Fig. S5), paired t-tests were used to test for differences in L4-evoked responses at maximum stimulus intensity.

Multiphoton CGH-based inhibitory output mapping

Laser light was generated using a 5W 1040 nm femtoTrain laser (Sepctra-Physics) and power was modulated on short time scales using a Pockels cell (Conoptics) and a high speed shutter (UniBlitz). Light was delivered to the sample using a VIVO 2- Photon workstation (3i) based on a Sutter Moveable Objective Microscope (Sutter) and the hologram was created using a Phasor 2-Photon computer-generated holography system (3i) with Slidebook software (3i) (Fig. S9a). The holograms used for stimulation were 2D discs of diameter 15 um centered on points with 20 um spacing, making a 400 um x 400 um grid in the focal plane (Fig. S9b,c). Stimulation consisted of 4 or 10 ms square pulses to the Pockels cell with voltages calibrated to produce 200 or 250 mW average power on sample, respectively. The choice of 4 ms at 200 mW or 10 ms at 250 mW stimulation was determined slice to slice based on opsin expression. Power for each hologram was calibrated empirically to account for power loss due to diffraction efficiency degradation away from the zero-order of the SLM. There was an inter-trial interval of 100 ms between the end of one stimulation and the start of the next stimulation. Under these conditions, SOM cells spiked reliably and with high radial resolution (Fig. 3c, Fig. S9c,d) and moderate axial resolution (Fig. S9f,g). Given the sparsity of SOM neurons (Fig. 3b), this level of spatial resolution provided a good tradeoff between sampling many cells with fewer targets and spiking cells with high

spatial resolution. In addition, reliably evoked spikes were produced with low latency and jitter when stimulating randomly through the target grid at 10 Hz. Under these conditions, most evoked spikes occurred in the first 20 ms after the onset of stimulation (Fig. S9e,h).

Space clamp error will inevitably affect somatic measurements of currents from distally located SOM→PC synapses; however, we recorded IPSCs using a cesium-based internal solution (which included the ion channel blockers tetraethylammonium and QX-314) and performed experiments at room temperature, which ameliorate this to some extent (Williams and Mitchell, 2008). We also used a holding potential of +40 mV to increase the IPSC driving force. In these experiments, internal solutions also contained 5 μM Alexa 488 hydrazide (ThermoFisher Scientific) to aid visualization with multiphoton imaging, and ~5 mM kynurenic acid Sodium salt (abcam) was added to the external ACSF to block glutamatergic activity.

To determine which locations evoked responses in the voltage-clamp recordings, first we detected IPSCs using a Bayesian modeling approach via Gibbs sampling (Merel et al., 2016). Event times were estimated by first binning all of the time samples at 1 ms resolution and then finding maxima of those timeseries (using *findpeaks* in MATLAB). Because the vast majority of evoked spikes recorded from opsin expressing SOM cells occurred with short latency (Fig. S9c,f), we estimated the background rate of IPSCs for each patched cell from the last 25 ms of all inter-trial intervals and the evoked rate at each location from a time window of 30 ms starting 5ms after the onset of each stimulation. Taking a Poisson distribution of events with the estimated background rate as a null distribution for all locations for each cell, we could then calculate a p-value for the hypothesis that there is no evoked IPSCs each location. We then

detected locations with evoked responses using the Benjamini-Hochberg False Detection Rate (FDR) procedure with q = 0.1 (Benjamini and Hochberg, 1995). We chose this relatively liberal FDR rate because any false positives will likely be thrown out after the temporal statistics are taken into account.

To determine if a location with evoked rates in both simultaneously patched cells was in fact a common input from a single source, we employed a statistical test that compares a computed synchrony statistic against a null distribution computed from resampled event time series. Specifically, the test we use employs a null distribution where all synchrony is a result of some processes at timescales longer than some given duration (Amarasingham et al., 2012). The intuition is that the chosen duration should match the general timing of evoked IPSCs such that any synchrony under this null arises only because IPSCs are being generated by two separate presynaptic SOM cells at roughly the same time. When we reject this null, we have evidence that the synchrony is coming from a process that operates at a finer timescale than the general evoked IPSC statistics: that is, a single presynaptic SOM cell is generating highly time-locked IPSCs in two postsynaptic PCs. In our case, the duration of the timescale we want to test against can be estimated from both the timing statistics of evoked spiking of SOM cells as wells as the peristimulus time histogram (PSTH) of IPSCs for all trials at all detected input locations across all PC input maps (Fig. S9e,h, Fig. S10g). Using these statistics as guidance, we chose 10 ms as the timescale for our null distribution. In detail, we first summarize the synchrony of events between two simultaneously patched cells at each location where both cells receive input. The statistic we use is the sum of the center and two flanking bins of the cross correlation of the binary event time series for each cell. As mentioned, the event time series are binned at 1 ms.

We then created a null distribution for this statistic at each of these locations using the event series resampling described in (Amarasingham et al., 2012) which allowed us to estimate a p-value for each location as well (Fig. S10h,i,j,k). We then detected common spatiotemporal input using these p-values and the Benjamini-Hochberg FDR procedure with q = .05, aggregating all tests across all paired maps. The common input probability for a simultaneously patched pair could then be computed as the total number of detected common input locations for that pair divided by the total number of unique detected input locations for the pair (i.e. the cardinality of the union of the sets of input locations for the two cells.

To align the input maps for each cell, we first aligned each input map to a two-photon image of the tissue taken at the time of recording based on previous calibrations between the SLM coordinate frame (e.g. the input map frame) and the two-photon imaging frame. Next, the tissue-aligned maps were then registered via an affine transform to a confocal image of the fixed slice which had been stained with DAPI and in which the opsin expressing cells could be visualized as well as the patched cells which had been filled with biocytin. This allowed each map to be registered to each other based on the laminar borders, in particular the L4-L5 boundary.

Biocytin staining and reconstruction

Following experiments, slices were transferred to 4% paraformaldehyde at 4° for several days. Slices were then repeatedly washed in TBS and subsequently incubated in block solution at room temperature for two hours. Next, 1:1000 streptavidin-Alexa647 conjugate was added to

the solution and allowed to stain for 2 hours. Slices were then washed again and mounted/DAPI-stained on coverslips using VectaShield.

Stained neurons were imaged on a confocal microscope, along with the DAPI signal in order to identify laminar boundaries. These images allowed us to qualitatively assess whether recorded cells were L1-targeting MCs or L4-targeting XCs. We reconstructed a subset of filled neurons, with the goal of performing a bulk quantification of how MC and XC neurites are distributed with respect to the cortical layers (Fig. 1c, Fig S2e). Since detailed reconstructions of the morphologies of these neurons have already been carried out by others (He et al., 2016; Ma et al., 2006; McGarry et al., 2010; Silberberg and Markram, 2007; Tan et al., 2008; Wang et al., 2004; Xu et al., 2013), we adopted a high-throughput, semi-automated approach to perform 2D reconstruct MCs and XCs (Fig. S2c). We imaged neurons using a 10x air objective and used the Imaris software package to automatically trace filled neurites. Subsequently, we manually edited these traces and annotated layer boundaries. These reconstructions did not distinguish between axon and dendrite and contained small scale errors (e.g. neurites passing near each other were sometimes spuriously connected). However, comparison of semi-automated reconstructions with detailed 3D reconstructions (performed manually in Imaris, after imaging with a 60x oil immersion objective and/or a 20x air objective) showed that the semi-automated approach yielded an accurate measurement of neurite density in each layer (Fig. S2a,b).

Supplemental Text

Comparison of L5 X94 cells and L4 non-Martinotti SOM cells

Unlike L5 non-Martinotti SOM cells, L4 non-Martinotti SOM cells (sometimes identified as low-threshold spiking or 'LTS' cells) are well described (Beierlein et al., 2000, 2003; Gibson et al.,

2005; Ma et al., 2006, 2012; Xu et al., 2013). Several lines of evidence suggest that these L4 non-Martinotti SOM cells belong to a similar or the same cell-type as the L5 cells labeled by the X94 line.

First, many L4 SOM cells are labeled by the X94 line. Like L5 X94 cells, these neurons are non-Martinotti cells with axons that target L4 rather than L1. Furthermore, L4 X94 cells have intrinsic properties which are very similar to those of L5 X94 cells (Fig S3 b-e). A recent study reported that the L4 SOM cells which are not labeled by X94 display the same phenotype as X94+ L4 SOM cells (Xu et al., 2013), suggesting that all or nearly all L4 SOM cells are X94-like, non-Martinotti cells.

Second, we observed that excitatory synapses from L4 PCs to L5 X94 cells exhibited what appeared to be asynchronous EPSCs during sustained high frequency firing in the presynaptic cell, which continued even after the cessation of presynaptic spiking (Fig. S8c). Elucidating the mechanism of this phenomenon was outside the scope of this study, but they can perhaps be attributed to asynchronous glutamatergic transmission. Asynchronous release of glutamate is uncommon in cortical circuits; to the best of our knowledge, the only other published observation is at the synapse from L4 PCs onto L4 SOM cells (Beierlein et al., 2003). Similarly, were also able to observe asynchronous IPSCs in L4PCs during sustained high frequency firing of a connected L5 XC.

Third, excitatory input mapping to L4 X94 cells revealed that these neurons receive input from the same locations as L5 X94 cells- L4 and the L5B/L6 border (Fig. S3f, h, j). Additionally, during L4 stimulation experiments, L4 X94 cells recorded at the same time as L5 X94 cells had almost

identical responses (Fig. S5), indicating similar degrees of L4 input to both L4 and L5 X94s. Furthermore, the connectivity of L5 X94s is broadly similar to the reported connectivity of L4 SOM cells, since both are densely interconnected with L4 PCs and L4 FS cells. The connectivity of L5 X94 cells does differ from that of L4 SOM cells in some respects. For example, L4FS cells appear to connect to L5 X94 cells less often than has been reported for L4FS→ L4SOM connections (Fig. S7a-c). Additionally, whereas L4SOM→L4FS synapses are also reported to be more powerful than L4SOM→L4PC synapses, we found that L5X94→L4PCand L5X94→ L4FS synapses evoked IPSPs/IPSCs of similar amplitudes (Fig. S7d-j), though our sample size was relatively limited.

Overall L4 SOM cells and L5 X94 cells exhibit strikingly similar electrophysiological, morphological, synaptic, and connective features, indicating that cells from both groups might be considered 'XCs'. Working under this assumption, roughly what fraction of SOM cells in the barrel cortex are XCs? The X94 line labels approximately 15% of SOM cells in the infragranular layers. This can be considered a lower bound on the fraction of XCs in L5, since the X94 line may not label all the cells with an XC phenotype, as is the case in L4. In the subset of L5 SOM-TdT cells that we filled with biocytin and could successfully recover the morphology, we found that 19/52 cells (37%) possessed XC morphologies, 31/52 (60%) possessed MC morphologies, and 2/52 could not be placed in either category. Consistent with this, a support vector machine trained to distinguish L5 GIN cells from L5 X94 cells based on their intrinsic properties (Fig. S1g) labeled X% of L5 SOM-TdT cells as putative XCs. However, L5 XCs often appeared to have larger cell bodies than MCs, which could potentially have made L5 XCs easier to locate or patch and thereby introduce a bias in this assessment. Thus it is likely that between 15-40% of L5 SOM

cells are XCs. L4 and L5 respectively host approximately 10% and 40% of all SOM cells in S1, so assuming nearly all L4 SOM cells are XCs, we estimate that L4 and L5 XCs represent 16-26% of all SOM cells in S1.

L4 GIN cells

Consistent with the idea that L4 SOM cells are nearly all non-Martinotti, we observed that L4 cells labeled by the GIN line also exhibited non-Martinotti morphologies (Fig. S3a). L4 GIN cells had intrinsic properties which were significantly different from those of L5 GIN (MC) cells, but similar to those of L4 X94 cells and L5 X94 (XC) cells (Fig. S3b-e). Furthermore, the excitatory input maps for L4 GIN cells showed that these neurons received laminar patterns of input very similar to those of L4 and L5 X94 cells, which were dominated by L4 input. The input maps of L4 X94 cells, L5 X94 cells, and L4 GIN cells were all significantly different than the input maps for L5 GIN MCs in terms of the fraction of input originating from L4 and L6 (Fig. S3g,I,j). These results indicate that L4 GIN cells are distinct from L5 GIN MCs. and suggest that L4 GIN cells can also be considered XCs on the basis of their similarities with X94 cells. Thus, while the GIN line primarily labels MCs in L5, it is more heterogeneous across all the cortical layers, labeling a mixture of MCs and XCs.

We exploited this fact in order to implement a paired experimental design for our L4 stimulation experiments. The aim of these experiments was to compare the amount of L4 input received by L5 XCs and L5 MCs, which required us to perform experiments in two sets of animals (SCNN1-Cre; X94 mice and SCNN1-Cre; GIN mice). Whenever possible, while recording from an L5 X94 (XC) or L5 GIN (MC), we also recorded simultaneously from an L4 X94 or L4 GIN

(both XCs). This configuration acts as a control for possible variability (e.g. in opsin expression, slice health) that is bound to occur to some extent between different slices and animals.

We observed that both L4 GIN cells and L4 X94 cells both received strong input during L4 photostimulation. Furthermore, we observed no significant difference in the responses of these two populations, indicating that we achieved the same degree of L4 activation in both experimental conditions ($p>0.05$ for EPSC charge transfer and spiking, for both types of photostimulation; F-test of linear mixed effects model coefficients). The responses of both L4 GIN and L4 X94 cells were similar to those of L5 X94 cells for all measures, suggesting that L4 provides a similar degree of drive to L4 XCs and L5 XCs (Fig. S5a-h).

In contrast, L5 GIN MCs received much less input from L4 than the other groups. In many conditions, we observed essentially no evoked excitation in L5 MCs; because we concurrently observed very strong excitation in L4 XCs, we can confidently conclude that this result is due to a near absence of L4PC→L5MC connectivity (Fig. S5a-h). When L5 GIN MCs did exhibit L4-evoked EPSCs (typically only during high intensity stimulation, Fig. S5c,d,i,j), their onset occurred at a considerably longer latency than in L5 XCs (Fig. 5k, 4.6 ms vs 3.6 ms; $p < 0.001$; two-sample t-test, $T(30) = -3.66$) suggesting that they were polysynaptic rather than monosynaptic.

Acknowledgements

We are grateful to Ariel Agmon (West Virginia University) for generously providing X94 mice. We thank Christopher Douglas, Desiree Chu, and Kirill Chesnov for technical assistance. We thank Ming-Chi Tsai, Alan Mardinly, Scott Pluta, Julia Veit, Evan Lyall, and Ian Oldenburg for

helpful comments and discussion. This work was supported by National Institute of Neurological Disorders and Stroke grant DP2NS087725-01 and the New York Stem Cell Foundation. A.N. is supported by the National Institute of Neurological Disorders and Stroke of the National Institutes of Health under Ruth L. Kirschstein National Research Service Award F31NS093925. B.M.S. is supported by a Fannie and John Hertz Foundation Fellowship and an NSF Graduate Research Fellowship. L.P. is supported by IARPA MICRONS contract D16PC00003 and DARPA SIMPLEX contract N66001-15-C-4032. H.A. is a New York Stem Cell Foundation Robertson Investigator.

Author contributions

Conceptualization, A.N. and H.A.; Methodology, A.N., B.M.S., L.P.; Investigation, A.N., B.M.S., B.S., and A.Y.E.; Resources, S.S.; Formal Analysis, A.N. and B.M.S.; Writing – Original Draft, A.N.; Writing – Review & Editing, A.N., B.M.S., L.P., and H.A.; Funding Acquisition, H.A.; Supervision, H.A. and L.P.

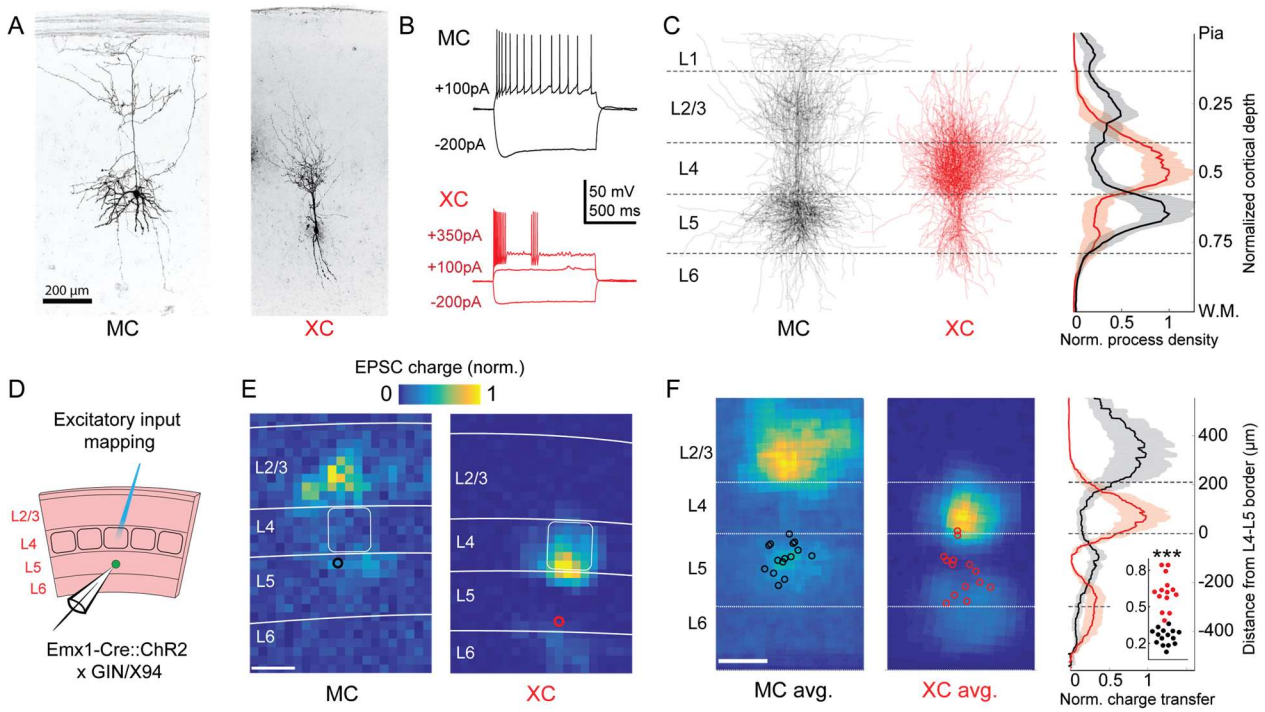

Figure 1. Optogenetic circuit mapping reveals complementary synaptic input patterns to two subtypes of L5 SOM cells.

(A) Confocal images of dye filled neurons revealing two morphological phenotypes of L5 SOM cells. Left: an L5 GIN cell. Right: an L5 X94 cell. Scale bar: 200 µm.

(B) Example traces during current step injections from an L5 GIN cell (black) and an L5 X94 cell (red).

(C) Left: Overlaid morphological reconstructions of L5 GIN/MC cells (black, n=14) and L5 X94/XC cells (red, n=10) showing differences in laminar distribution of neurites. Right: Normalized neurite density versus cortical depth for L5 GIN (black) and L5 X94 cells (red). Data are represented as mean ± C.I.

(D) Schematic of experimental configuration. A digital micromirror device was used to focally photo-stimulate excitatory cells in different regions of the slice in order to map the spatial profile of excitatory inputs to GFP+ L5 MCs (Emx1-Cre; GIN) or GFP+ L5 XCs (Emx1-Cre; X94).

(E) Example heat maps of median EPSC charge transfer evoked at each stimulus site for example L5 SOM cells. Left: An L5 MC that received inputs from L5 and L2/3. Right: An L5 XC that received inputs from L4 and the L5/6 border. Soma locations are indicated by red/black bordered white dot). Scale bar: 200 µm.

(F) Left: Grand averages of input maps reveal cell-type specific patterns of laminar input. Soma locations are indicated as above. Right: Normalized charge transfer versus distance from L4-L5 border for MC (black) and XC (red) populations. Scale bar: 200 µm.

Inset: Swarm plots showing the proportion of total evoked charge transfer in each map that originated from sites in L4+L6, i.e. [L4+L6] / [L2/3+L4+L5+L6] for the MC (black; median, 27%; range, 13-36%) and XC (red; median, 62%; range, 38-84%) populations. Proportions were significantly different between L5 MCs and L5 XCs (25 ± 3% in n = 15 MCs versus 62 ± 7% in n = 14 XCs, mean ± C.I.; $p = 6.5 \cdot 10^{-10}$; two-sample t-test)

See also Figures S1-4.

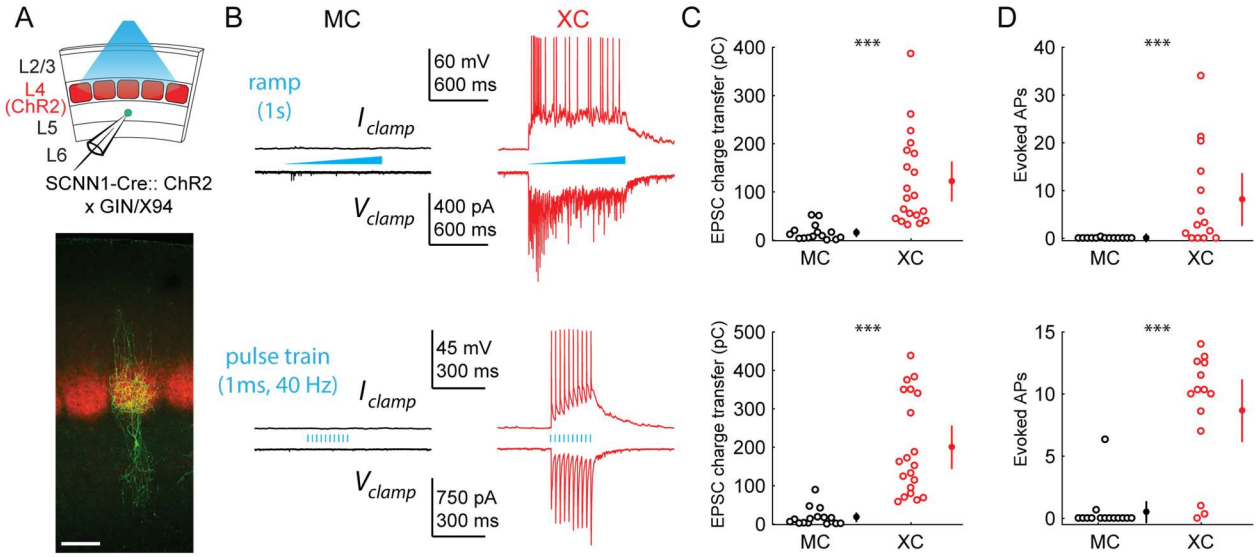

Figure 2. L4 photo-stimulation excites L5 XCs but not L5 MCs

(A) Top: Schematic of the experimental configuration. L5 X94 or GIN cells were recorded during photo-stimulation of L4 excitatory neurons. Bottom: Confocal image of a filled L5 X94 neuron (green) with ChR2-TdTomato expression (red) visible in L4. Scale bar: 150 µm.

(B) Top row: Example traces recorded in the current clamp (upper traces) or voltage clamp (lower traces) configurations during a 1-second ramp photo-stimulation. Bottom row: As above, but for photo-stimulation with a 40 Hz train of ten 1ms pulses.

(C) Quantification of excitatory charge transfer during maximum intensity 1-second ramp stimulation trials. Mean 122 ± 41 pC in n = 20 XCs versus 15 ± 8 pC in n = 15 MCs; $p = 3.9 \cdot 10^{-6}$, Wilcoxon rank sum test.

(D) Quantification of the mean number of evoked action potentials during maximum intensity 1-second ramp stimulation trials. Mean 8.1 ± 5.5 spikes per trial in n = 15 XCs versus 0.03 ± 0.05 spikes per trial in n = 15 MCs; $p = 6.6 \cdot 10^{-4}$, Wilcoxon rank sum test.

(E) As in C, for maximum intensity 40Hz pulse train stimulation. Mean 200 ± 56 pA in n = 20 XCs versus 18 ± 12 pA in n = 15 MCs; $p = 2.8 \cdot 10^{-6}$, Wilcoxon rank sum test.

(F) As in D, for maximum intensity 40Hz pulse train stimulation. Mean 8.7 ± 2.4 spikes per trial in n = 15 XCs versus 0.5 ± 0.9 spikes per trial in n = 15 MCs; $p = 1.5 \cdot 10^{-6}$, Wilcoxon rank sum test.

Error bars denote mean ± 95% confidence interval. Three asterisks denotes $p<0.001$. See also Figure S5.

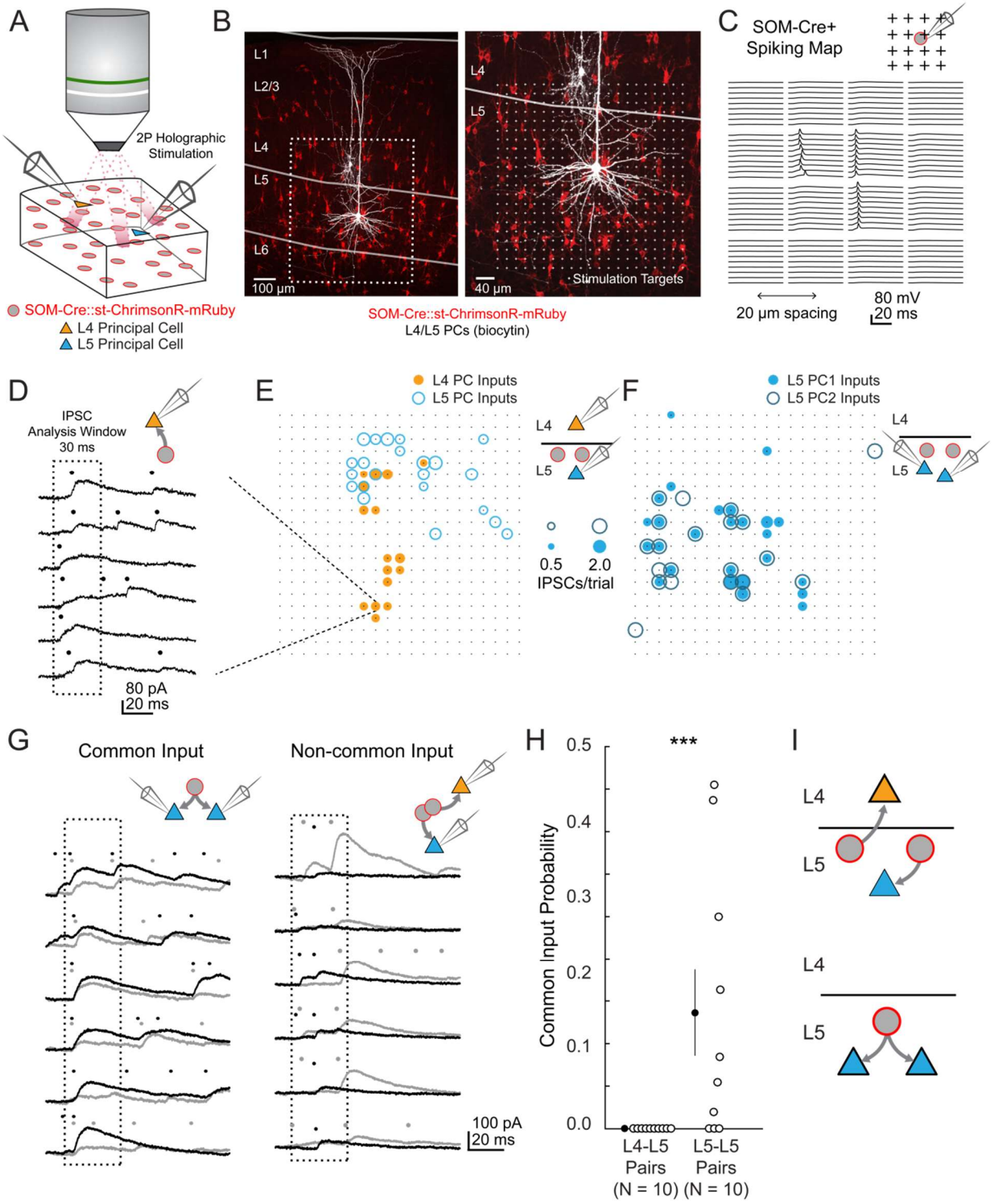

Figure 3. 2 photon optogenetic circuit mapping reveals that L4 and L5 PCs are inhibited by separate populations of L5 SOM cells.

(A) Schematic of the experimental configuration. IPSCs are recorded from a pair of PCs (either an L4/L5 pair or an L5/L5 pair) while SOM cells expressing soma-targeted ChrimsonR-mRuby2 are focally activated using 2P photo-stimulation and computer generated holography.

(B) Left: post-hoc confocal image showing SOM cells expressing soma-targeted-ChrimsonR-mRuby2 (red) and biocytin fills of recorded PCs in L4 and L5 (white) at 10x magnification. Right: Confocal image at 20x magnification showing the grid of photo-stimulated target locations. Both images are max z-projections over 100 µm.

(C) Spatial photo-excitation profile of a soma-targeted-ChrimsonR-mRuby2 expressing SOM cell. Whole cell current-clamp recordings from this cell showing multiple trials of photo-stimulation at a 4 x 4 subsection of the photo-stimulation grid with 20 µm spacing between stimulation locations. The SOM cell is recruited to spike only at a small number of stimulation sites, but does so reliably and with low jitter across trials at these sites.

(D) Example traces showing IPSCs recorded from an L4 PC during SOM photo-stimulation at a single site (corresponding to black boxed square in E) over multiple trials. Dots above each trace indicate the onset time of detected IPSCs ($p = .0003$, Poisson detection).

(E) Example overlay of maps showing the mean number of IPSCs at detected input locations during photo-stimulation for a simultaneously recorded L4 PC-L5 PC pair. Bubble size indicates the mean number of IPSCs evoked (deviation from background rate) per trial.

(F) As in E, but for an L5 PC-L5 PC pair.

(G) Example traces illustrating method for detection of common SOM-mediated inputs to pairs of simultaneously recorded PCs. Left: IPSC traces at a single site recorded simultaneously in two PCs (each PC is indicated by black or grey traces) and corresponding detected IPSCs. IPSCs with synchronous onset occur in many trials, despite the trial-to-trial jitter in IPSC onset, suggesting that a SOM cell which diverges onto both recorded PCs is being stimulated at this site ($p = .0005$, synchrony jitter test). Right: IPSC traces from a different site. Evoked IPSCs are observed in both cells, but the lack of synchronicity suggests they arise from separate, neighboring SOM cells ($p = .4$). Dots above each trace indicate the estimated onset time of detected IPSCs.(H) Probability of detecting common SOM input per photo-stimulated site for pairs consisting of L4 PCs and L5 PCs versus pairs consisting of two L5 PCs. No common input locations were detected in $n = 10$ L4-L5 pairs versus 13.7 ± 5.1% of all input locations locations stimulated in $n = 10$ L5-L5 pairs; $p = 1.1 \cdot 10\text{-}3$, Wilcoxon rank sum test Data are summarized by mean ± S.E.M.

(I) Schematic of main result for SOM outputting mapping. Individual L5 SOM cells form inhibitory connections onto L4 PCs and or L5 PCs but not both. See also Figure S9, S10.

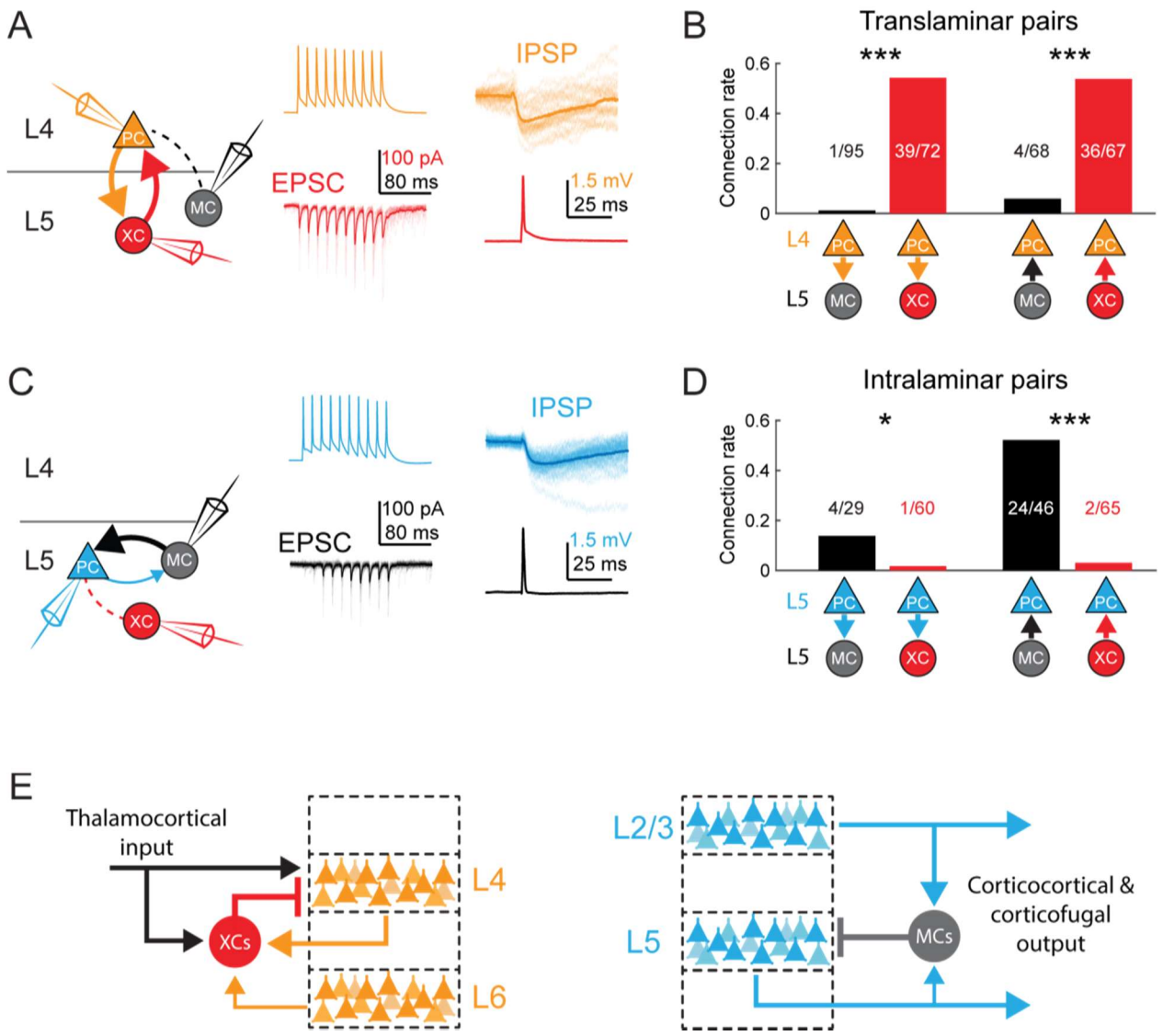

Figure 4. MCs and XCs exhibit different patterns of monosynaptic connectivity with L4 and L5 PCs.

(A) Paired recordings of L4 PCs (orange) and L5 XCs/MCs (red/black).). Left: schematic of the tested circuit. Middle: example traces of evoked spikes in a L4 PC (orange) and the excitatory synaptic current in a L5 XC (red). Right: example traces of evoked IPSPs in a L4 PC (orange) in response to a single action potential in a L5 XC (red).

(B) Bar graph summarizing translaminar connection rates between L4 PCs and L5 MCs (black bars) and L4 PCs and L5 XCs (red bars). $p < 10^{-6}$ for L4PC→L5MC (n = 95 connections tested onto 39 MCs) versus L4PC→L5XC connection rate (n = 72 connections tested onto 51 XCs); $p = 2 \cdot 10^{-6}$ for L5MC→L4PC (n = 68 connections tested from 35 MCs) versus L5XC→L4PC connection rate (n = 67 connections tested from 51 XCs); Monte Carlo permutation test.

(C) As in A, but intralaminar pairs between L5 MCs/XCs and L5 PCs (blue).

(D) As in B, but for intralaminar connections with L5 PCs. $p = 0.020$ for L5PC→L5MC ($n = 29$ connections tested onto 20 MCs) versus L5PC→L5XC connection rate ($n = 60$ connections tested onto 35 XCs); $p<10^{-6}$ for L5MC→L5PC ($n = 46$ connections tested from 30 MCs) versus L5XC→L5PC connection rate ($n = 65$ connections tested from 37 XCs); Monte Carlo permutation test.

(E) Schematic overview of the circuit architecture supported by data in this study. L5 SOM cell subtypes participate in at least two distinct circuits. Left: L5 XCs receive local excitatory input mainly from L4 and L6, and inhibit L4, indicating that L5 XCs provide feedforward and feedback inhibition during the early stages of cortical processing. XCs also receive thalamocortical input (Tan et al., 2008). Right: L5 MCs receive excitatory inputs from PCs in L2/3 and L5, and inhibit L5 PCs, providing feedback inhibition to major output channels of the cortical microcircuit.

See also Figures S6-8 and Table S1.

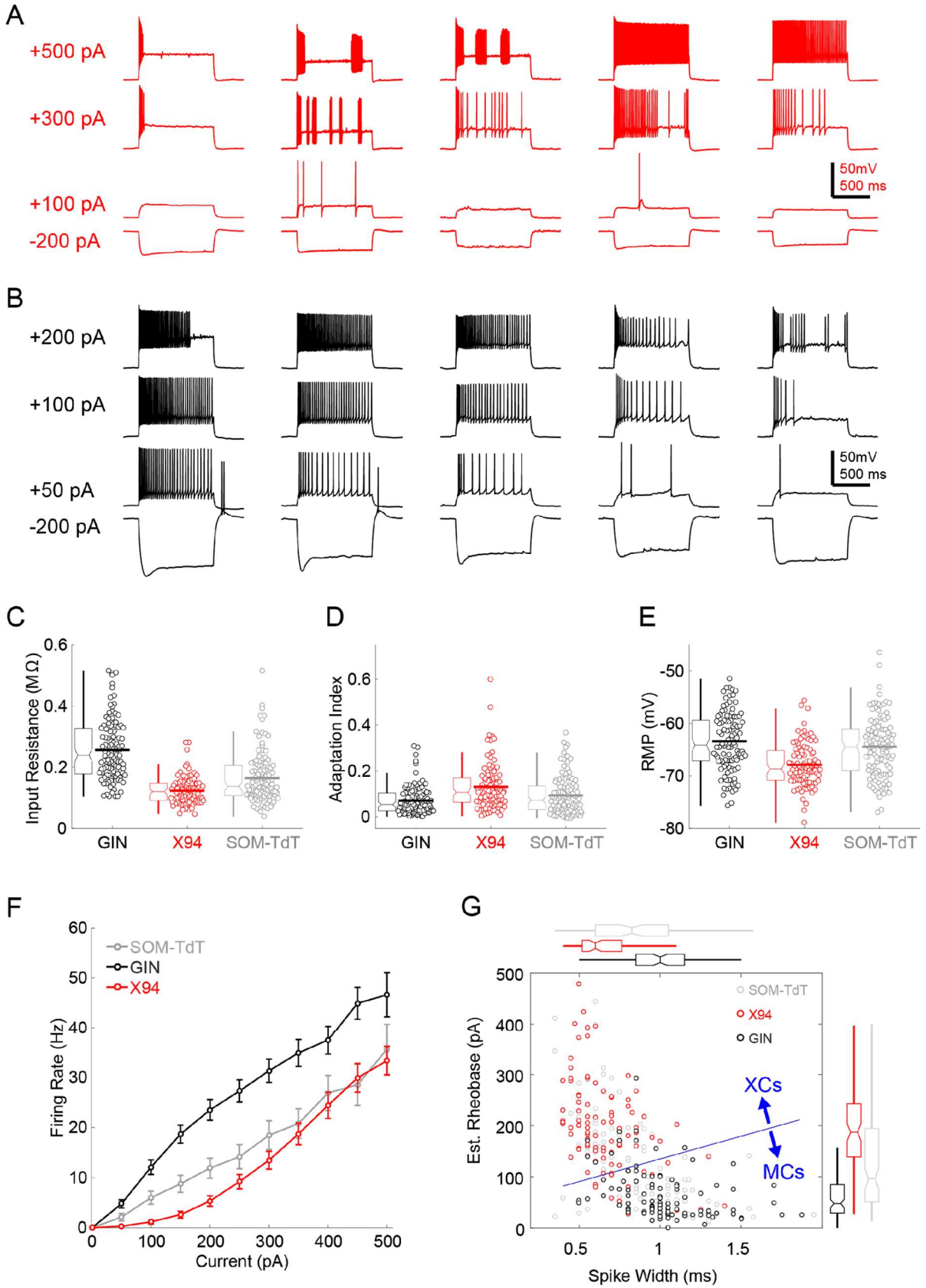
A
+500 pA
+300 pA
+100 pA
-200 pA
50mV
500 ms
B
+200 pA
+100 pA
+50 pA
-200 pA
50mV
500 ms
C
Input Resistance (MΩ)
GIN
X94
SOM-TdT
D
Adaptation Index
GIN
X94
SOM-TdT
E
RMP (mV)
GIN
X94
SOM-TdT
F
SOM-TdT
GIN
X94
Firing Rate (Hz)
Current (pA)
G
SOM-TdT
X94
GIN
XCs
MCs
Est. Rheobase (pA)
Spike Width (ms)

Supplemental Figure 1. Intrinsic properties of L5 SOM cells; related to Figure 1.

(A) Example traces showing diverse spiking responses of L5 X94 cells during current injection.

(B) As in A, but for L5 GIN cells. Note that less current is being injected due to the greater input resistance of these cells.

(C) Swarm and box-and-whisker plots of input resistance for L5 GIN cells (black), L5 X94 cells (red), and L5 SOM-TdT cells (gray). Thick horizontal line indicates distribution mean.

(D,E) As in C, but for spike frequency adaptation index and resting membrane potential.

(F) FI curves from L5 cells recorded in the SOM-TdT line (gray), GIN line (black), or X94 line (red).

(G) Scatter plot showing estimated rheobase and median spike width for L5 GIN cells (black), L5 X94 cells (red), and L5 SOM-TdT cells (gray). Box and whisker plots summarizing population statistics for these variables are in the margins. The blue line indicates the decision boundary for a linear support vector machine trained to classify L5 GIN cells and L5 X94 cells based on these two variables; this classifier was in turn used to classify SOM-TdT cells as putative XCs or MCs.

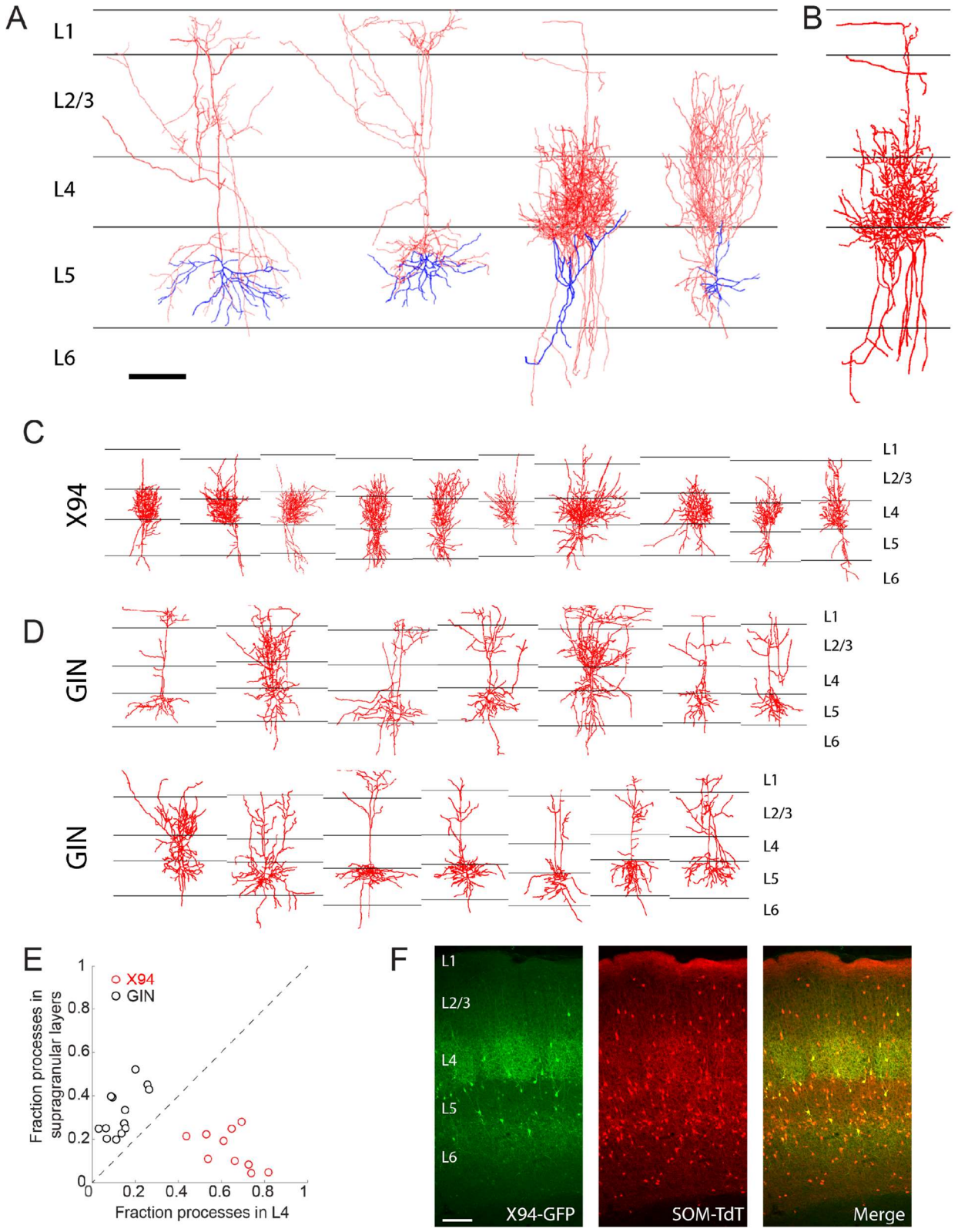

Supplemental Figure 2. Morphological reconstruction of L5 SOM cells; related to Figure 1.

(A) Examples of biocytin reconstructions done manually at high magnification of two L5 MCs (left two) and two L5 XCs (right two) showing axonal (red) and dendritic (blue) morphology. Scale bar 150 µm.

(B) An example of a semi-automated reconstruction done at 10x magnification of an L5 XC (compare to the third reconstruction in A).

(C) Semi-automated reconstructions of L5 X94 cells

(D) As in C, but for L5 GIN cells.

(E) Comparison of neurite density of L5 GIN cells and L5 X94 cells in L4 versus the supragranular layers.

(F) Coronal section of barrel cortex in an X94-GFP; SOM-TdT mouse. TdTomato fluorescence can be seen in all layers, with a dense band in L1 from the axons of MCs. Dense axonal arborization of X94-GFP cells is visible in L4, and upper L6 to a lesser extent, but not in L1.

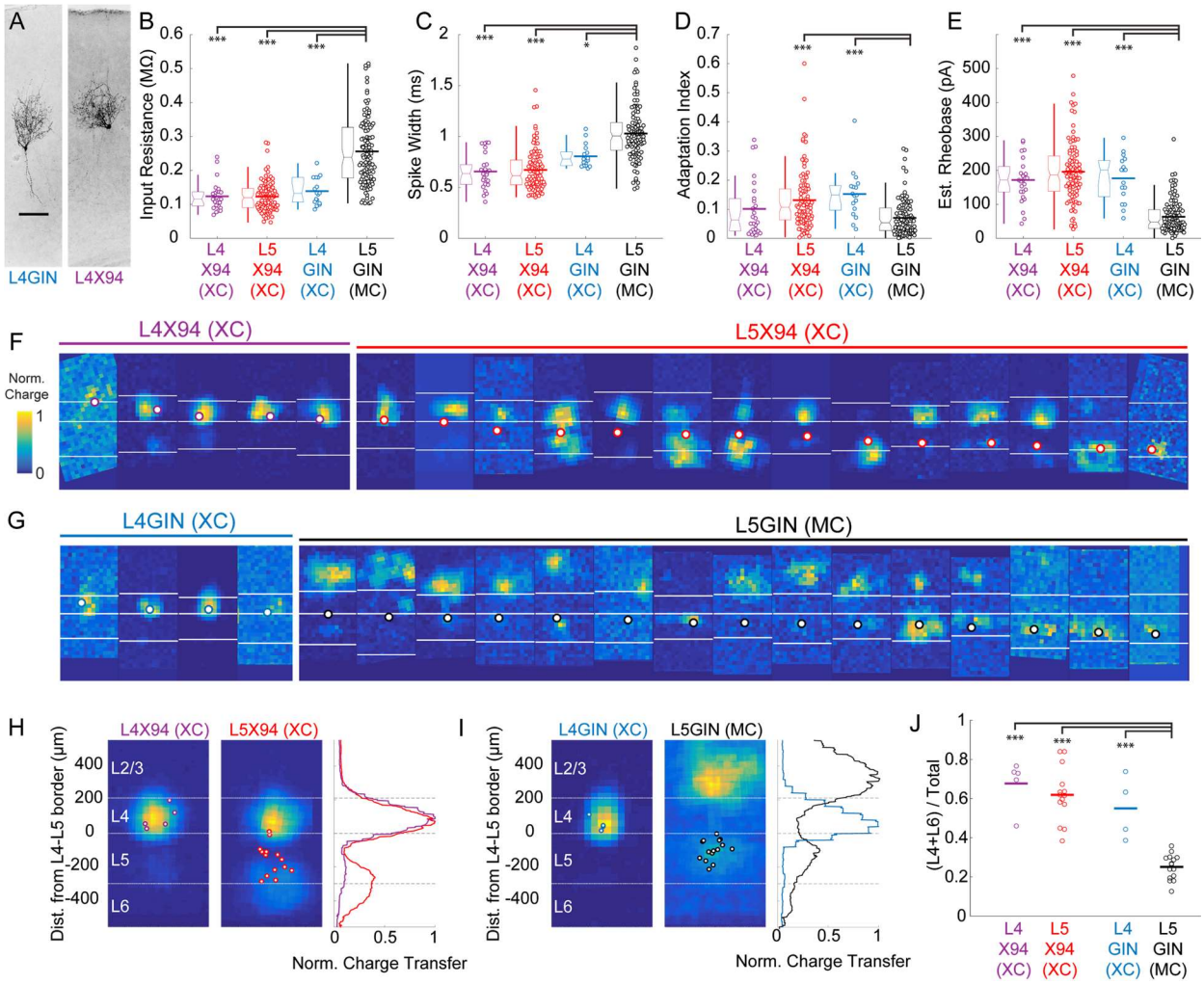

Supplemental Figure 3. Comparison of intrinsic properties and excitatory inputs for L4 and L5 SOM cells; related to Figure 1.

(A) Biocytin fills of an L4 GIN cell (left) and an L4 X94 cell (right), both exhibiting non-Martinotti morphology.

(B) Input resistances for L4X94, L5 X94, L4 GIN, and L5 GIN populations. Data are displayed as swarm plots, accompanied by Tukey box plots. The thick horizontal bar within the swarm indicates population mean. The L4 X94, L4 GIN, and L5 X94 populations have significantly lower input resistances than the L5 GIN population (L4 X94, $p = 3.8 \cdot 10^{-9}$; L5 X94, $p = 3.8 \cdot 10^{-9}$; L4 GIN, $p = 3.8 \cdot 10^{-5}$; Wilcoxon rank-sum test versus L5 GIN population).

(C) As in B, but for spike width. The L4 X94, L4 GIN, and L5 X94 populations have significantly shorter spike widths than the L5 GIN population (L4 X94, $p = 4.0 \cdot 10^{-9}$; L5 X94, $p = 3.8 \cdot 10^{-9}$; L4 GIN, $p = 0.029$; Wilcoxon rank-sum test versus L5 GIN population).

(D) As in B, but for adaptation index score. The L4 GIN and L5 X94 populations have significantly shorter spike widths than the L5 GIN population (L5 X94, $p = 1.5 \cdot 10^{-6}$; L4 GIN, $p = 1.4 \cdot 10^{-4}$; Wilcoxon rank-sum test) but the L4 X94 was not significantly different.

(E) As in B, but for estimated rheobase. The L4 X94, L4 GIN, and L5 X94 populations have significantly shorter spike widths than the L5 GIN population (L4 X94, $p = 7.2 \cdot 10^{-9}$; L5 X94, $p = 3.8 \cdot 10^{-9}$; L4 GIN, $p = 6.4 \cdot 10^{-7}$; Wilcoxon rank-sum test versus L5 GIN population).

(F) All excitatory input maps for X94 cells in L4 (left, orange) and L5 (right, red). Bordered white dots indicate the location of the recorded soma. **G**. As in F, but for GIN cells in L4 (gray) and L5 (black).

(H) Average maps for L4 and L5 XCs. Both groups receive strong input from L4. L5 XCs receive stronger inputs on average from the infragranular layers, though there was no significant difference between these groups nor a significant correlation of the depth of the recorded cell with the relative amount of input received from the deeper layers.

(I) As in H, but for GIN cells. L4 GIN cells (XCs) receive inputs primarily from L4 (similar to X94 cells) and are very different from L5 GIN cells (MCs).

(J) L5 GIN MCs received a significantly smaller proportion of excitatory charge transfer originating from L4 and L6 than other cell types (L4 X94, $p = 7.2 \cdot 10^{-9}$; L5 X94, $p = 3.8 \cdot 10^{-9}$; L4 GIN, $p = 6.4 \cdot 10^{-7}$; Wilcoxon rank-sum test versus L5 GIN population).

Single asterisk indicates $p<0.05$, three asterisks indicates $p<0.001$.

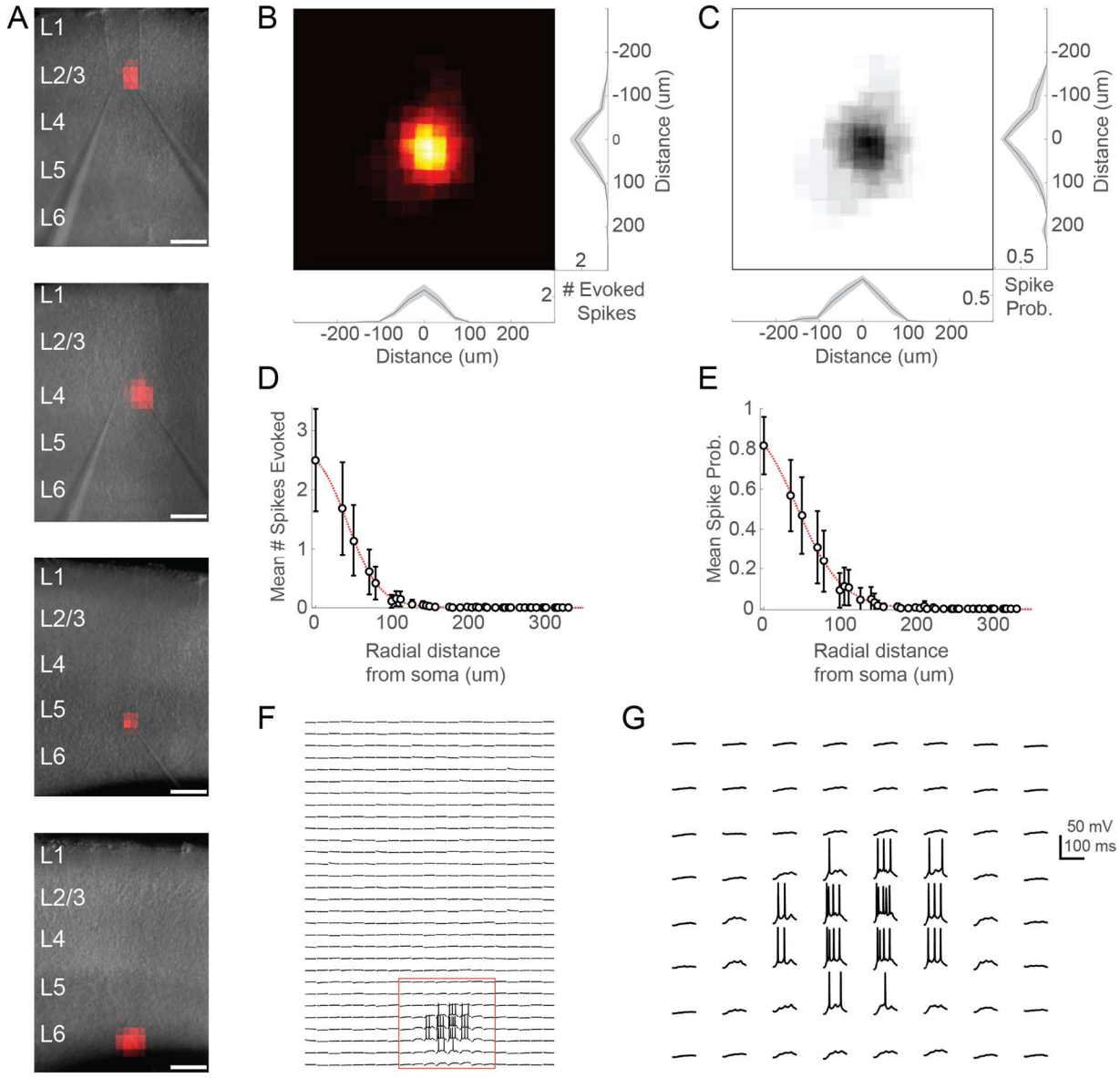

Supplemental Figure 4. Excitation profiles of ChR2+ cells in Emx-Cre DMD-based one photon optogenetic mapping experiments; related to Figure 1.

(A) Example spiking heatmaps recorded from cells in L2-6, overlaid on infrared images of slices. Scale bar indicates 175µm.

(B) Average map of # of evoked spikes per trial in n= 20 ChR2+ cells. Maps are centered on the somata of recorded cells.

(C) As in B, but for probability of evoking at least 1 spike per trial.

(D) Average number of spikes evoked as a function of radial distance from ChR2+ cell soma.

(E) As in D, but for probability of evoking at least one spike.

(F) Example traces corresponding to the bottom heatmap in A. Spiking is evoked only during perisomatic photostimulation.

(G) Expanded view of red boxed region in F. Bursts of spikes are evoked in a single trial during direct stimulation of the soma.

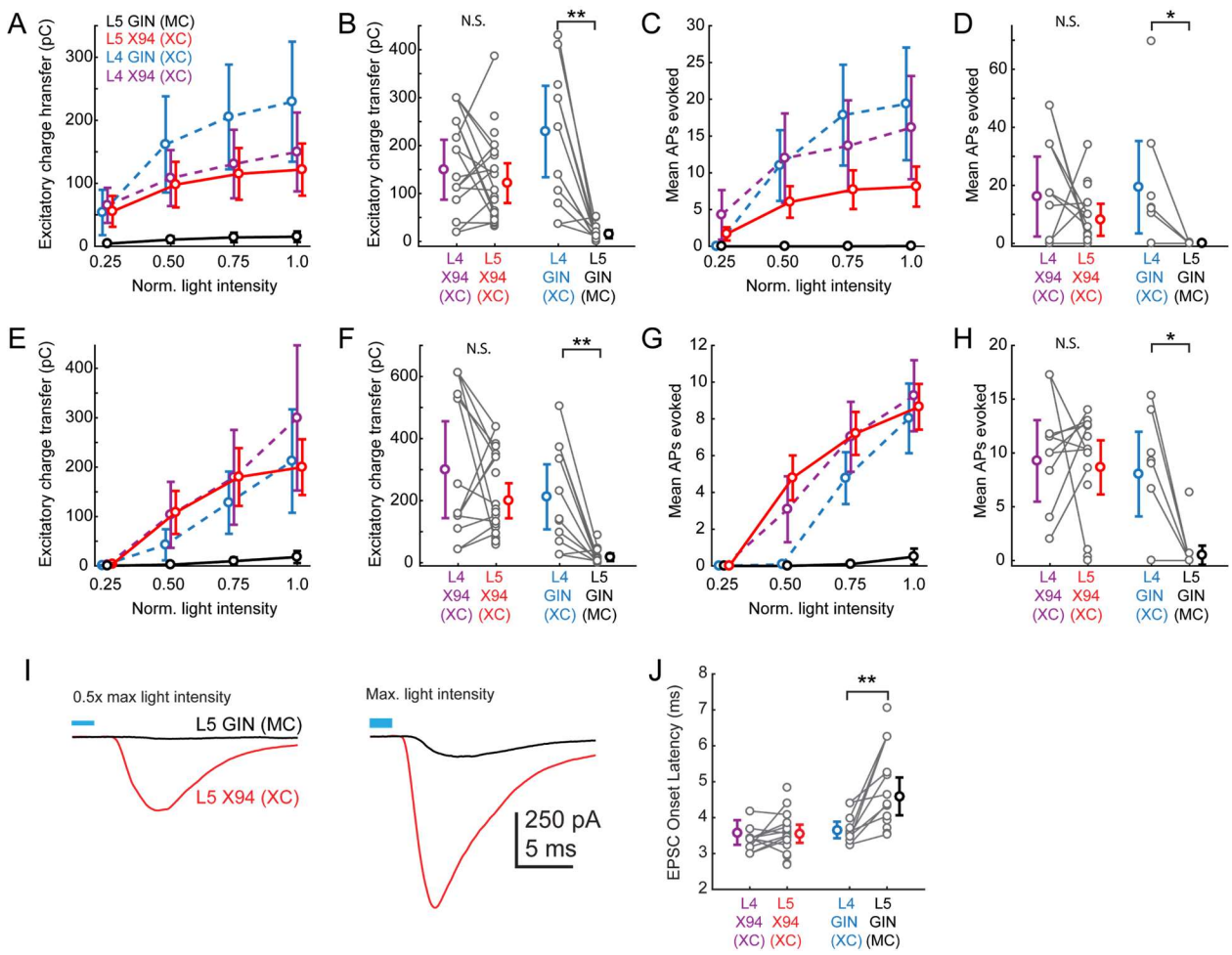

Supplemental Figure 5. Responses of L4 and L5 SOM cells to L4 photo-stimulation; related to Figure 2.

(A) Dose response profile of excitatory charge transfer evoked during 1 second ramp stimulation of L4 for X94 cells in L4 (purple) and L5 (red) and for GIN cells in L4 (blue) and L5 (black). To assess differences between groups, we fit a linear mixed-effects model with fixed effects parameters for the slope of the stimulus-response function and random effects slope parameters for each slice and cell recorded, along with a single intercept term. The L5 GIN cell group had a significantly lower fixed effects slope coefficient than the L5 X94 ($p = 2.1 \cdot 10^{-5}$), L4 X94 ($p = 3.1 \cdot 10^{-5}$), and L4 GIN groups ($p = 2.0 \cdot 10^{-9}$).

(B) Mean excitatory charge transfer evoked during maximum intensity 1 second ramp stimulation of L4. Gray lines indicate pairs of cells recorded in the same slice. Charge transfer was not significantly different between L4 X94 cells and L5 X94 cells on a pairwise basis (169.1 ± 91.5 pC versus 118.7 ± 44.0 pC ; p = 0.10, paired t-test), but was significantly different between L4 GIN cells and L5 GIN cells (229.4 ± 95.3 pC versus 15.2 ± 8.4 pC; p = 0.002, paired t-test).

(C,D) As in A,B, but for mean number of action potentials evoked in L5 SOM cells recorded in current clamp during 1 second ramp photo-stimulation. F-tests on coefficients of a linear mixed-model indicated that the L5 GIN cell group had a significantly lower fixed effects slope coefficient than the L5 X94 ($p = 0.03$), L4 X94 ($p = 1.0 \cdot 10^{-3}$), and L4 GIN groups ($p = 1.7 \cdot 10^{-4}$). The mean number of spikes evoked was not significantly different between L4 X94 cells and L5 X94 cells on a pairwise basis (20.4 ± 23.7 spikes versus 9.0 ± 6.0 spikes ; $p = 0.14$, paired t-test), but was significantly different between L4 GIN cells and L5 GIN cells (19.4 ± 16.0 spikes versus 0.03 ± 0.05 spikes; $p = 0.034$, paired t-test).

(E,F). As in A,B, but for excitatory charge transfer in L5 SOM cells recorded in voltage clamp during a train of ten 1ms pulses at 40 Hz. F-tests on coefficients of a linear mixed-model indicated that the L5 GIN cell group had a significantly lower fixed effects slope coefficient than the L5 X94 ($p = 1.2 \cdot 10^{-6}$), L4 X94 ($p = 3.5 \cdot 10^{-9}$), and L4 GIN groups ($p = 5.2 \cdot 10^{-16}$). Charge transfer was not significantly different between L4 X94 cells and L5 X94 cells on a pairwise basis (309.1 ± 220.6 pC versus 191.5 ± 58.8 pC ; $p = 0.055$, paired t-test), but was significantly different between L4 GIN cells and L5 GIN cells (212.2 ± 104.7 pC versus 18.0 ± 12.2 pC; $p = 0.002$, paired t-test).

(G,H). As in A,B, but for mean number of action potentials evoked in L5 SOM cells recorded in current clamp during a train of ten 1ms pulses at 40 Hz. F-tests on coefficients of a linear mixed-model indicated that the L5 GIN cell group had a significantly lower fixed effects slope coefficient than the L5 X94 ($p = 1.2 \cdot 10^{-6}$), L4 X94 ($p = 5.3 \cdot 10^{-9}$), and L4 GIN groups ($p = 2.2 \cdot 10^{-14}$). The mean number of spikes evoked was not significantly different between L4 X94 cells and L5 X94 cells on a pairwise basis (9.8 ± 6.2 spikes versus 8.6 ± 2.6 spikes; $p = 0.56$, paired t-test), but was significantly different between L4 GIN cells and L5 GIN cells (8.0 ± 3.9 spikes versus 0.5 ± 0.9 spikes; $p = 0.0068$, paired t-test).

(I) Plots of the grand average EPSC evoked at mild intensity (top; 0.625 $mW \cdot mm^2$) pulse and maximum intensity stimulation (bottom; 1.25 $mW \cdot mm^2$) of L4 for L5 MCs (black) and L5 XCs (red). Low intensity stimulation produced robust EPSCs in L5 XCs but not L5 MCs. High intensity stimulation was able to evoke EPSCs L5 MCs but with a delayed onset.

(J) Plot of average EPSC onset latency in response to maximum intensity pulse stimulation of L4 (as seen in bottom panel of I) in different SOM cell populations. Gray dots indicate individual cells in each group; cells connected by gray lines indicate neurons recorded in the same preparation (usually simultaneously). EPSC onset latency is uniformly longer for L5 MCs compared to paired L4 XCs.

Errorbars indicate mean ± confidence interval.

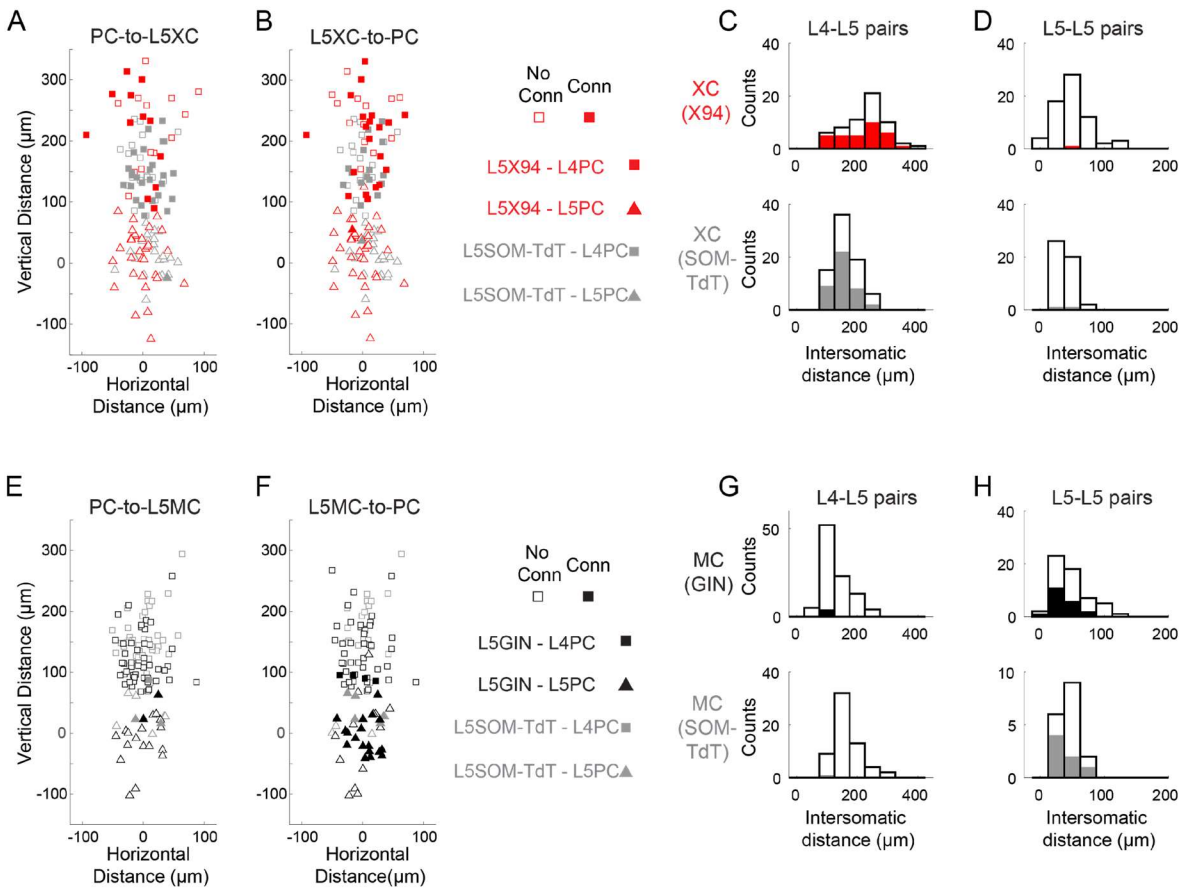

Supplemental Figure 6. Distances of connections tested in paired recordings; related to Figure 4.

(A) Scatterplot showing the relative distances between pairs tested for monosynaptic excitatory connections from L4 and L5 PCs onto L5 XCs. Squares represent L5XC-L4 PC pairs; triangles represent L5XC-L5 PC pairs. Filled markers indicate that a connection was observed; open markers indicate no connection was observed. Red symbols indicate pairs tested in X94 mice; gray symbols indicate pairs tested in SOM-TdT mice where the L5 XC was identified electrophysiologically. The origin represents the position of the L5 XC soma (note that these were located at variable distances from the L4-L5 border).

(B) As in A, but for monosynaptic inhibitory connections from L5 XCs onto L4 and L5 PCs.

(C) Histogram showing the distribution of intersomatic distances between pairs of L5 XCs and L4 PCs. Empty bars indicate the number of pairs tested per binned distance; filled bars indicate the number of positive connections (unidirectional in either direction or bidirectional) detected at that bin. Top: pairs in X94 mice. Bottom: pairs in SOM-TdT mice.

(D) As in C, but for pairs of L5 XCs and L5 PCs.

(E-H) As in A-D, but for pairs of L5 MCs and L4/L5 PCs. Other than the layer-specific connectivity biases of MCs and XCs, we did not observe any significant relationship between intersomatic distance (vertical, horizontal, or Euclidean) and connection probability.

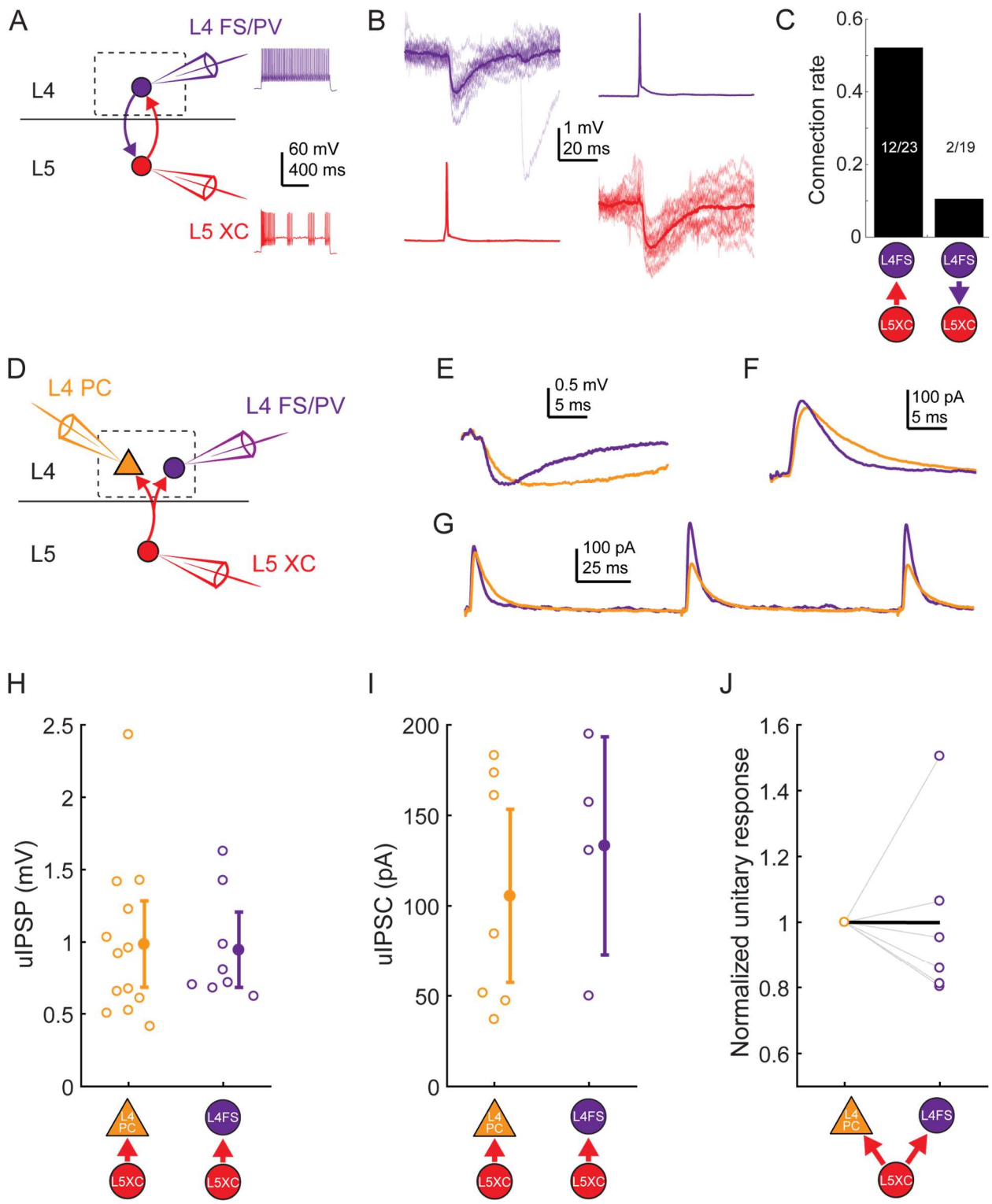

Supplemental Figure 7. L5 XC connectivity onto L4 FS cells; related to Figure 4.

(A) Schematic of paired recordings between L4 FS/PV cells (purple) and L5 XCs. Inset: example spiking in response to depolarizing current injection.

(B) Monosynaptic IPSPs could be observed in L4 FS cells in response to single spikes in L5 XCs (left) and vice versa (right)

(C) Bar graph showing connection rates for L5XC-L4FS pairs. Connections from L5 XCs onto L4 FS cells were observed frequently, whereas connections from L4 FS cells onto L5 XCs occurred rarely.

(D) In some experiments, divergence from L5 XCs was observed by holding one L5 XC while serially patching L4 PCs and L4 FS/PV cells.

(E) Example IPSPs in an L4 PC and L4 FS/PV cell evoked by the same L5 XC.

(F) As in E, but while using a Cs-based internal to record IPSCs (holding potential +10mV) in an L4 PC and an L4 FS/PV cell.

(G) As in F, but while evoking multiple spikes in the L5 XC at 10 Hz.

(H) Amplitude of unitary IPSPs evoked by L5 XCs in L4 PCs (0.98 ± 0.30 mV) and L4 FS cells (0.94 ± 0.26 mV). Summary data are represented as mean ± 95% C.I.

(I) Amplitude of unitary IPSCs (recorded using cesium-based internal solution) evoked by L5 XCs in L4 PCs (105 ± 48 pA) and L4 FS cells (133 ± 60 pA). Summary data are represented as mean ± 95% C.I.

(J) Comparison of unitary response amplitudes (IPSPs or IPSCs) for pairs in which serial recordings were established for an L5XC-to-L4PC connection (left) and an L5XC-to-L4FS/PV connection (right), normalized to the amplitude of the L4PC response. Thick black line connects the mean normalized L4 PC unitary response (by definition, 1) and mean normalized L4 FS/PV unitary response (0.99 ± 0.52).

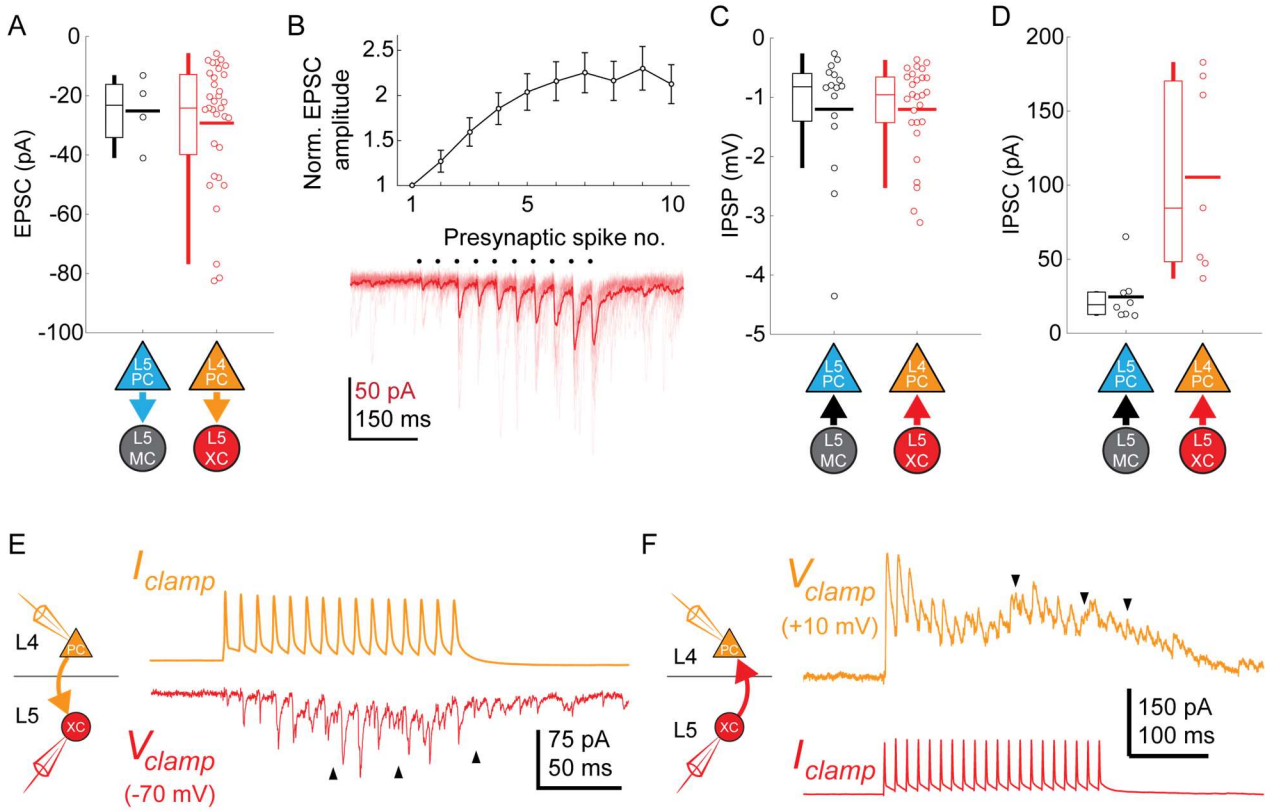

Supplemental Figure 8. Synaptic properties of L5 SOM connections; related to Figure 4.

(A) Swarm plots and Tukey box plots of evoked EPSC amplitude in connections onto L5 MCs (black) and L5 XCs (red), measured as the largest EPSC evoked during a train of presynaptic firing at 70 Hz.

(B) Facilitation dynamics of EPSCs onto L5 XCs. Bottom: example of facilitating EPSCs in response to a train of 10 spikes at 70 Hz in an L4 PC. Top: Mean EPSC amplitude evoked in L5XCs while stimulating L4 PCs at 70 Hz, normalized to EPSC amplitude after the initial spike. Errorbars represent mean ± S.E.M.

(C) Swarm plots and Tukey box plots of evoked IPSP amplitude in connections from L5 MCs (black) and L5 XCs (red) onto L4/L5 PCs.

(D) As in D, but for IPSCs recorded in L4/L5 PCs (holding potential +10mV) using a Cs-based internal. Unlike IPSPs, IPSCs evoked by L5XCs onto L4PCs are stronger than those evoked by L5 MCs onto L5 PCs; this may reflect differences in space clamp error when recording from L4 PCs vs L5 PCs.

(E) Sustained high frequency spiking in L4 PCs appeared to evoke asynchronous EPSCs in L5 XCs (indicated by black arrows) which continued even after the cessation of spiking.

(F) As in C, but for L5XC-to-L4PC connections. Sustained high frequency spiking in L5XCs appeared to evoke asynchronous IPSCs in L4 PCs (indicated by black arrows) which continued even after the cessation of spiking.

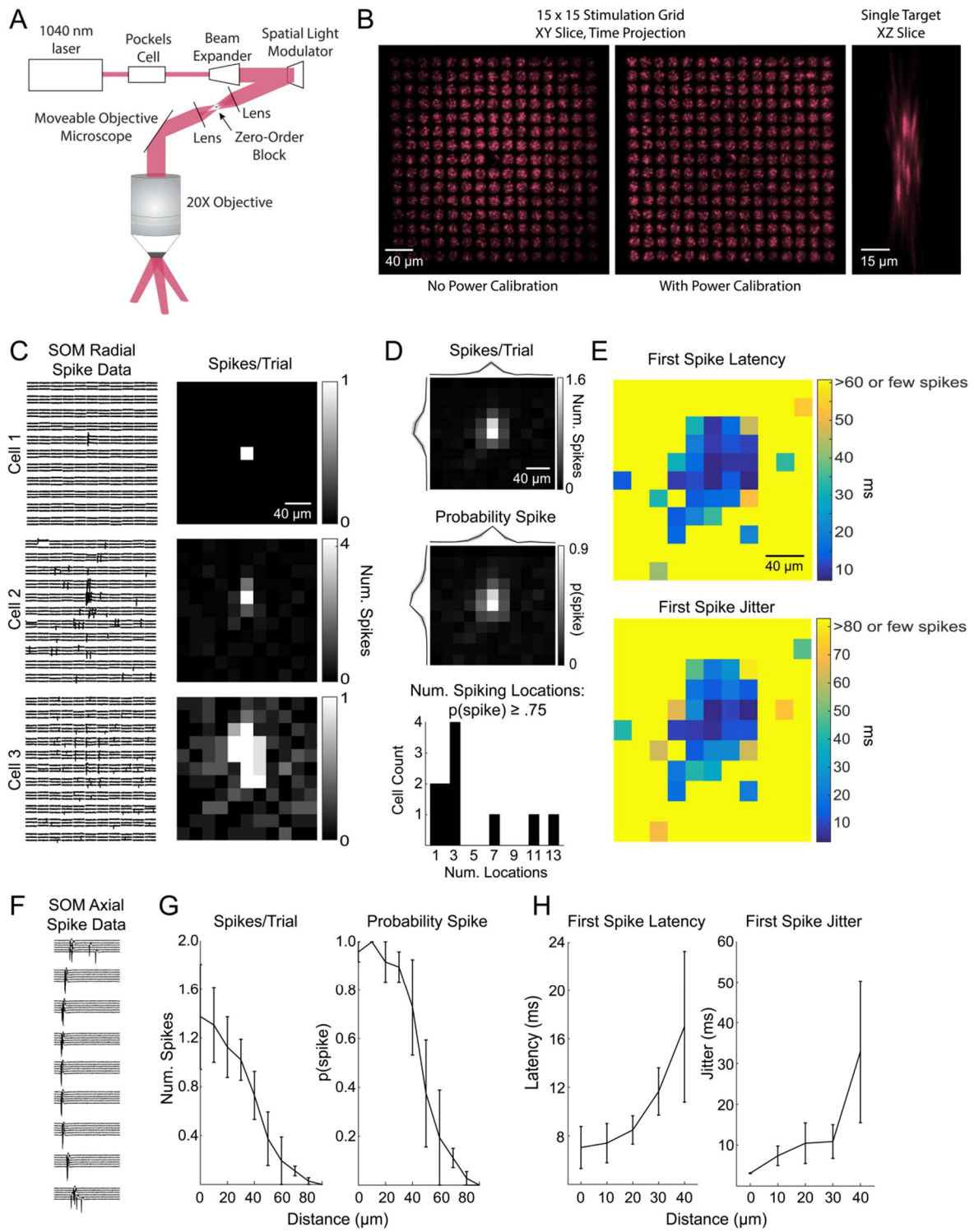

Supplemental Figure 9. Excitation profiles of st-ChrimsonR-expressing SOM cells in multiphoton holographic SOM-Cre mapping experiments; related to Figure 3.

(A) Schematic of the CGH-based stimulation microscope.

(B) Imaging stimulation holograms with two-photon induced fluorescence in a thin fluorescent slide. Left: Time projection of a stimulation sequence covering a 15 x 15 grid of targets at 20 µm spacing before power calibration. Middle: As in Left but with power calibration. Left: XZ slice of a single target. Note that excitation is confined to a small volume and that power calibration results in more uniform excitation radially. The decrease in fluorescence in the middle of the two stimulation grids is due to the zero-order block.

(C) Example plots of the lateral resolution of photo-stimulation. Left column: Raw cell-attached data of light-evoked spiking for example SOM cells. Right column: average number of spikes evoked per trial at each location. Locations are 20 µm apart as in mapping experiments.

(D) Radial spike count statistics. Top: Average map of the number of evoked spikes per trial in st-ChrimsonR+ cells (n= 11). Maps are centered on the somata of recorded cells. Middle: As in top, but for probability of evoking at least 1 spike per trial. Bottom: Histogram of number of locations per cell which evoked a spike at least 75% of the trials.

(E) Radial spike timing statistics. Top: Average first spike latency for st-ChrimsonR+ cells (n = 11). Yellow indicates that the average was > 60 ms or that too few spikes were observed across cells at those locations to obtain a good estimate. Bottom: Average first spike jitter, computed as the full-width half-maximum of the first spike times. Yellow indicates a jitter of greater than 80 msec or that too few spikes were observed across cells at those locations.

(F) Data from an example cell as the hologram is moved axially. Distance between locations is 10 µm.

(G) Axial spike count statistics. Left: Average number of evoked spikes as a function of axial distance for st-ChrimsonR+ cells (n=4). Right: As in left, but for the probability of at least one spike per trial.

(H) Axial spike timing statistics. Left: Average first spike latency as a function of axial distance (n=4 cells). Right: First spike jitter as a function of axial distance for st-ChrimsonR+ cells (n = 3).

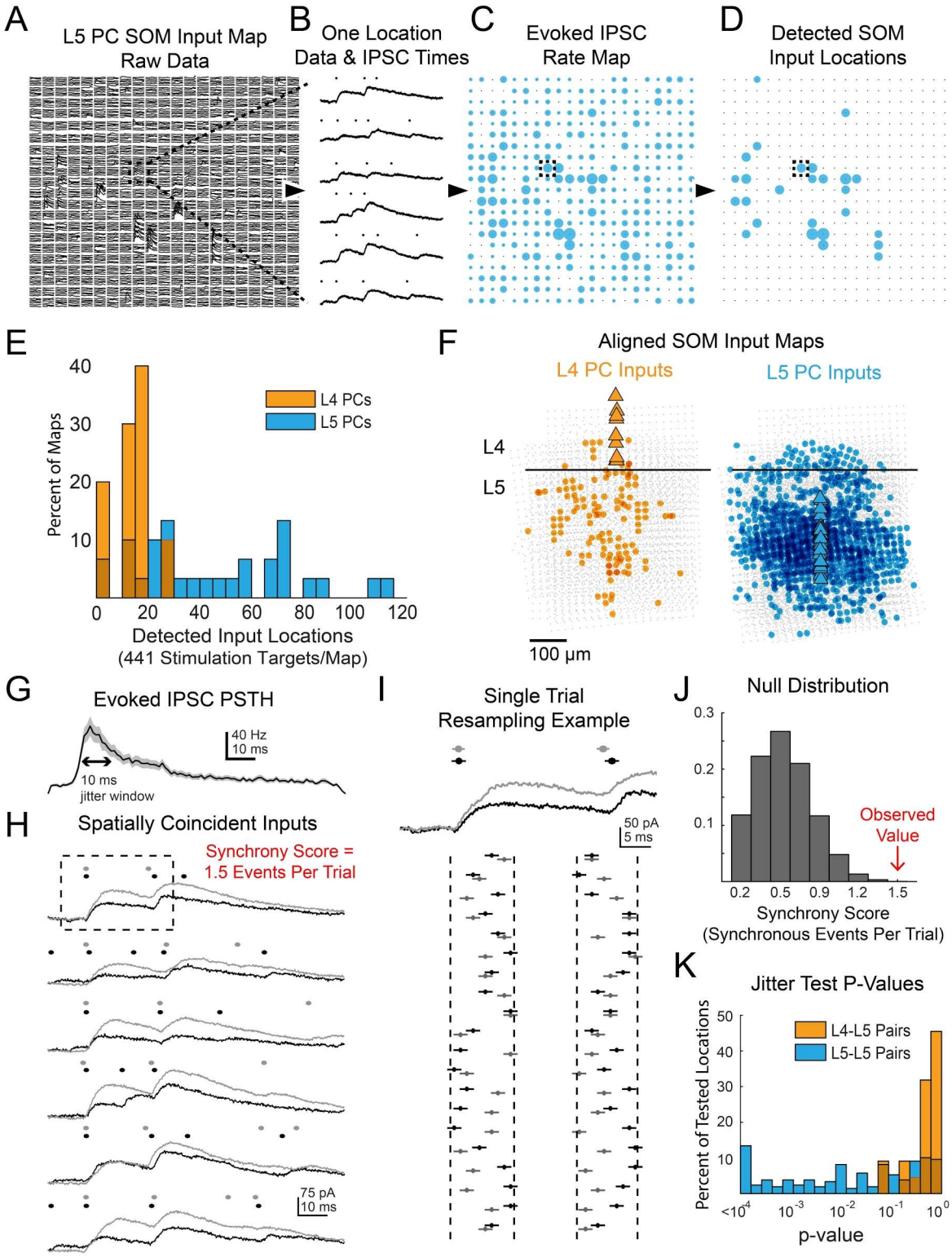
A
L5 PC SOM Input Map
Raw Data
B
One Location
Data & IPSC Times
C
Evoked IPSC
Rate Map
D
Detected SOM
Input Locations
E
Percent of Maps
L4 PCs
L5 PCs
Detected Input Locations
(441 Stimulation Targets/Map)
F
Aligned SOM Input Maps
L4 PC Inputs
L5 PC Inputs
L4
L5
100 µm
G
Evoked IPSC PSTH
40 Hz
10 ms
10 ms
jitter window
H
Spatially Coincident Inputs
Synchrony Score =
1.5 Events Per Trial
75 pA
10 ms
I
Single Trial
Resampling Example
50 pA
5 ms
J
Null Distribution
Observed
Value
Synchrony Score
(Synchronous Events Per Trial)
K
Jitter Test P-Values
L4-L5 Pairs
L5-L5 Pairs
Percent of Tested Locations
p-value

Supplemental Figure 10. Data processing and additional results for multiphoton SOM output mapping; related to Figure 3.

(A) Example of raw data a single map onto a L5 PC. Dashed box shows location for which data is shown in B.

(B) Example of Bayesian PSC detection on all 6 trials from a single location from the map in A.

(C) A map showing the evoked IPSC rates at each location for the map from A. Dashed box shows location of data from B.

(D) As in C except only locations which pass FDR detection are shown.

(E) Histograms showing the number of locations with evoked IPSCs for both L4 and L5 PCs.

(F) Overall spatial input distributions for SOM cells in L5 to both L4 PCs (left, n = 10) and L5 PCs (right, n = 28). Maps are aligned vertically to the L4-L5 border and horizontally to the PC soma. For this representation all inputs are plotted with the same size circle.

(G). PSTH of IPSC times aggregated from all locations with detected evoked IPSC rates. A 10 ms duration which matches the jitter duration for temporal synchrony is marked for comparison.

(H) As in B except showing data and IPSC detection for two simultaneously recorded L5 PCs. The synchrony score for this location is 1.5 events/trial. Dashed box shows data used for I.

(I) Example of 20 resamplings of the events during the analysis window for the first trial shown in H. Vertical dashed lines show discrete event jittering windows. Horizontal lines on each event span 2ms such that if the lines from two events overlap then they would be counted as synchronous.

(J) Null distribution of synchrony score from event time series resampling of the data in H. The observed value is from the far right extreme of the distribution.

(K) Histograms of p-values for all spatially overlapping locations for all pairs from jitter synchrony tests.

	GIN + X94			GIN + X94 + classified SOM-TdT			All SOM-TdT
	MCs	XCs	p	MCs	XCs	p	
L5SOM→L4PC	**4/47** **9%** 2/20 10%	**21/34** **62%** 18/28 64%	$1.6 \cdot 10^{-4}$	**4/68** **6%** 2/35 6%	**36/67** **54%** 31/51 61%	$2.0 \cdot 10^{-5}$	**15/55** **27%** 33/86 38%
L4PC→L5SOM	**0/50** **0%** 0/17 0%	**13/27** **48%** 11/23 48%	$5.8 \cdot 10^{-4}$	**1/95** **1%** 1/39 3%	**39/72** **54%** 31/51 61%	$<10^{-5}$	**27/91** **30%** 32/90 36%
L5SOM→L5PC	**19/38** **50%** 13/23 57%	**1/38** **3%** 1/24 4%	$2.8 \cdot 10^{-4}$	**24/46** **52%** 17/30 57%	**2/65** **3%** 2/37 4%	$<10^{-5}$	**6/35** **17%** 19/67 28%
L5PC→L5SOM	**2/22** **9%** 2/13 15%	**0/33** **0%** 0/22 0%	0.1431	**4/29** **14%** 4/20 20%	**1/60** **2%** 1/35 3%	0.02	**3/34** **9%** 5/55 9%

Supplementary Table 1. Connection rates for MCs and XCs recorded in different transgenic lines; related to Figure 4. Left columns show paired recording data collected using the GIN and X94 lines to respectively target MCs and XCs in L5. Right columns show the same data and additionally include data collected using the SOM-TdT line, with L5 SOM cells classified as putative MCs or XCs based on their intrinsic properties. Note that in many cases, more than one connection was tested per L5 SOM cell recorded i.e. one SOM cell can belong to multiple pairs. Bolded text at the top of each cell shows the number and fraction of SOM-PC pairs in which a monosynaptic connection was detected for a given condition; regular font shows the number and fraction of SOM cells tested in which at least one monosynaptic connection was observed for a given condition (for example, 39 connections were observed out of 72 connections tested from L4 PCs onto L5 XCs, with 31 out of 51 L5 XCs receiving at least one L4 PC connection.)

References

Adesnik, H., and Scanziani, M. (2010). Lateral competition for cortical space by layer-specific horizontal circuits. Nature *464*, 1155–1160.

Adesnik, H., Bruns, W., Taniguchi, H., Huang, Z.J., and Scanziani, M. (2012). A neural circuit for spatial summation in visual cortex. Nature *490*, 226–231.

Amarasingham, A., Harrison, M.T., Hatsopoulos, N.G., and Geman, S. (2012). Conditional modeling and the jitter method of spike resampling. J. Neurophysiol. *107*, 517–531.

Anastasiades, P.G., Marques-Smith, A., Lyngholm, D., Lickiss, T., Raffiq, S., Kätzel, D., Miesenböck, G., and Butt, S.J.B. (2016). GABAergic interneurons form transient layer-specific circuits in early postnatal neocortex. Nat. Commun. *7*, 10584.

Apicella, A.J., Wickersham, I.R., Seung, H.S., and Shepherd, G.M.G. (2012). Laminarly orthogonal excitation of fast-spiking and low-threshold-spiking interneurons in mouse motor cortex. J. Neurosci. *32*, 7021–7033.

Atallah, B. V, Bruns, W., Carandini, M., and Scanziani, M. (2012). Parvalbumin-expressing interneurons linearly transform cortical responses to visual stimuli. Neuron *73*, 159–170.

Atencio, C.A., Sharpee, T., and Schreiner, C.E. (2009). Hierarchical computation in the canonical auditory cortical circuit. Proc. Natl. Acad. Sci. *106*, 21894–21899.

Baker, C.A., Elyada, Y.M., Parra-Martin, A., and Bolton, M. (2016). Cellular resolution circuit mapping in mouse brain with temporal-focused excitation of soma-targeted channelrhodopsin. Elife *5*, 1–15.

Beierlein, M., Gibson, J.R., and Connors, B.W. (2000). A network of electrically coupled interneurons drives synchronized inhibition in neocortex. Nat. Neurosci. *3*, 904–910.

Beierlein, M., Gibson, J.R., and Connors, B.W. (2003). Two dynamically distinct inhibitory networks in layer 4 of the neocortex. J. Neurophysiol. *90*, 2987–3000.

Benjamini, Y., and Hochberg, Y. (1995). Controlling the False Discovery Rate : A Practical and Powerful Approach to Multiple Testing Author (s): Yoav Benjamini and Yosef Hochberg Source : Journal of the Royal Statistical Society . Series B (Methodological), Vol . 57 , No . 1 Published by : J. R. Stat. Soc. *57*, 289–300.

Berger, T.K., Perin, R., Silberberg, G., and Markram, H. (2009). Frequency-dependent disynaptic inhibition in the pyramidal network: a ubiquitous pathway in the developing rat neocortex. J. Physiol. *587*, 5411–5425.

Berger, T.K., Silberberg, G., Perin, R., and Markram, H. (2010). Brief bursts self-inhibit and correlate the pyramidal network. PLoS Biol. *8*.

Bock, D.D., Lee, W.-C.A., Kerlin, A.M., Andermann, M.L., Hood, G., Wetzel, A.W., Yurgenson, S.,

Soucy, E.R., Kim, H.S., and Reid, R.C. (2011). Network anatomy and in vivo physiology of visual cortical neurons. Nature *471*, 177–182.

Bortone, D.S., Olsen, S.R., and Scanziani, M. (2014). Translaminar inhibitory cells recruited by layer 6 corticothalamic neurons suppress visual cortex. Neuron *82*, 474–485.

Brill, J., Mattis, J., Deisseroth, K., and Huguenard, J.R. (2016). LSPS/Optogenetics to Improve Synaptic Connectivity Mapping: Unmasking the Role of Basket Cell Mediated Feed-Forward Inhibition. eNeuro *3*, ENEURO.0142-15.2016.

Buchanan, K.A., Blackman, A. V., Moreau, A.W., Elgar, D., Costa, R.P., Lalanne, T., Tudor Jones, A.A., Oyrer, J., and Sjöström, P.J. (2012). Target-Specific Expression of Presynaptic NMDA Receptors in Neocortical Microcircuits. Neuron *75*, 451–466.

Carandini, M., and Heeger, D. (2012). Normalization as a canonical neural computation. Nat. Rev. Neurosci. 1–12.

Cobas, a, Welker, E., Fairén, a, Kraftsik, R., and Van der Loos, H. (1987). GABAergic neurons in the barrel cortex of the mouse: an analysis using neuronal archetypes. J. Neurocytol. *16*, 843–870.

Constantinople, C.M., and Bruno, R.M. (2013). Deep cortical layers are activated directly by thalamus. Science *340*, 1591–1594.

Cottam, J.C.H., Smith, S.L., and Häusser, M. (2013). Target-specific effects of somatostatin-expressing interneurons on neocortical visual processing. J. Neurosci. *33*, 19567–19578.

DeNardo, L.A., Berns, D.S., DeLoach, K., and Luo, L. (2015). Connectivity of mouse somatosensory and prefrontal cortex examined with trans-synaptic tracing. Nat. Neurosci. 1–13.

Fairén, A. (2007). Cajal and Lorente de Nó on cortical interneurons: Coincidences and progress. Brain Res. Rev. *55*, 430–444.

Fairén, A., Cobas, A., and Fonseca, M. (1986). Times of generation of glutamic acid decarboxylase immunoreactive neurons in mouse somatosensory cortex. J. Comp. Neurol. *251*, 67–83.

Fanselow, E.E., Richardson, K.A., and Connors, B.W. (2008). Selective , State-Dependent Activation of Somatostatin-Expressing Inhibitory Interneurons in Mouse Neocortex. J. Neurophysiol. *100*, 2640–2652.

Feldmeyer, D. (2012). Excitatory neuronal connectivity in the barrel cortex. Front. Neuroanat. *6*, 24.

Fino, E., and Yuste, R. (2011). Dense inhibitory connectivity in neocortex. Neuron *69*, 1188–1203.

Fino, E., Packer, A.M., and Yuste, R. (2013). The logic of inhibitory connectivity in the neocortex. Neuroscientist *19*, 228–237.

Fu, Y., Tucciarone, J.M., Espinosa, J.S., Sheng, N., Darcy, D.P., Nicoll, R. a., Huang, Z.J., and Stryker, M.P. (2014). A cortical circuit for gain control by behavioral state. Cell *156*, 1139–1152.

Gibson, J.R., Beierlein, M., and Connors, B.W. (2005). Functional Properties of Electrical Synapses Between Inhibitory Interneurons of Neocortical Layer 4. J Neurophysiol *93*, 467–480.

Halabisky, B., Shen, F., Huguenard, J.R., and Prince, D.A. (2006). Electrophysiological classification of somatostatin-positive interneurons in mouse sensorimotor cortex. J. Neurophysiol. *96*, 834–845.

Harris, K.D., and Shepherd, G.M.G. (2015). The neocortical circuit: themes and variations. Nat. Neurosci. *18*, 170–181.

Hattox, A.M., and Nelson, S.B. (2007). Layer V neurons in mouse cortex projecting to different targets have distinct physiological properties. J. Neurophysiol. *98*, 3330–3340.

He, M., Tucciarone, J., Lee, S., Nigro, M.J., Kim, Y., Levine, J.M., Kelly, S.M., Krugikov, I., Wu, P., Chen, Y., et al. (2016). Strategies and tools for combinatorial targeting of GABAergic neurons in mouse cerebral cortex. Neuron 1–16.

Helmstaedter, M., Sakmann, B., and Feldmeyer, D. (2009). Neuronal Correlates of Local, Lateral, and Translaminar Inhibition with Reference to Cortical Columns. Cereb. Cortex *19*, 926–937.

Hilscher, M.M., Le, R.N., Edwards, S.J., Le, K.E., and Kullander, K. (2016). Chrna2-Martinotti Cells Synchronize layer 5 type A Pyramidal Cells via Rebound Excitation. 1–26.

Hofer, S.B., Ko, H., Pichler, B., Vogelstein, J., Ros, H., Zeng, H., Lein, E., Lesica, N.A., and Mrsic-Flogel, T.D. (2011). Differential connectivity and response dynamics of excitatory and inhibitory neurons in visual cortex. Nat. Neurosci. *14*, 1045–1052.

Hu, H., and Agmon, A. (2016). Differential Excitation of Distally versus Proximally Targeting Cortical Interneurons by Unitary Thalamocortical Bursts. J. Neurosci. *36*, 6906–6916.

Hu, H., Cavendish, J.Z., and Agmon, A. (2013). Not all that glitters is gold: off-target recombination in the somatostatin–IRES-Cre mouse line labels a subset of fast-spiking interneurons. Front. Neural Circuits *7*, 1–4.

Ji, X.Y., Zingg, B., Mesik, L., Xiao, Z., Zhang, L.I., and Tao, H.W. (2016). Thalamocortical Innervation Pattern in Mouse Auditory and Visual Cortex: Laminar and Cell-Type Specificity. Cereb. Cortex *26*, 2612–2625.

Jiang, X., Wang, G., Lee, A.J., Stornetta, R.L., and Zhu, J.J. (2013). The organization of two new cortical interneuronal circuits. Nat. Neurosci. *16*, 210–218.

Jiang, X., Shen, S., Cadwell, C.R., Berens, P., Sinz, F., Ecker, A.S., Patel, S., and Tolias, A.S. (2015).

Principles of connectivity among morphologically defined cell types in adult neocortex. Science (80-.). *350*, aac9462-aac9462.

Kapfer, C., Glickfeld, L.L., Atallah, B. V, and Scanziani, M. (2007). Supralinear increase of recurrent inhibition during sparse activity in the somatosensory cortex. Nat. Neurosci. *10*, 743–753.

Karnani, M.M., Agetsuma, M., and Yuste, R. (2014). A blanket of inhibition: functional inferences from dense inhibitory connectivity. Curr. Opin. Neurobiol. *26*, 96–102.

Karnani, M.M.M., Jackson, J., Ayzenshtat, I., Tucciarone, J., Manoocheri, K., Snider, W.G.G., and Yuste, R. (2016). Cooperative Subnetworks of Molecularly Similar Interneurons in Mouse Neocortex. Neuron *90*, 86–100.

Kato, H.K., Gillet, S.N., and Isaacson, J.S. (2015). Flexible Sensory Representations in Auditory Cortex Driven by Behavioral Relevance. Neuron *88*, 1027–1039.

Kätzel, D., and Miesenböck, G. (2014). Experience-Dependent Rewiring of Specific Inhibitory Connections in Adult Neocortex. PLoS Biol. *12*.

Kätzel, D., Zemelman, B. V, Buetfering, C., Wölfel, M., and Miesenböck, G. (2011). The columnar and laminar organization of inhibitory connections to neocortical excitatory cells. Nat. Neurosci. *14*, 100–107.

Kawaguchi, Y. (1993). Groupings of nonpyramidal and pyramidal cells with specific physiological and morphological characteristics in rat frontal cortex. J. Neurophysiol. *69*, 416–431.

Kepecs, A., and Fishell, G. (2014). Interneuron cell types are fit to function. Nature *505*, 318–326.

Kim, D., Jeong, H., Lee, J., Ghim, J., Her, E.S., Lee, S., Kim, D., Jeong, H., Lee, J., Ghim, J., et al. (2016). Distinct Roles of Parvalbumin- and Somatostatin- Expressing Interneurons in Working Memory Article Distinct Roles of Parvalbumin- and Somatostatin-Expressing Interneurons in Working Memory. Neuron *92*, 1–14.

Kim, E.J., Juavinett, A.L., Kyubwa, E.M., Jacobs, M.W., and Callaway, E.M. (2015). Three Types of Cortical Layer 5 Neurons That Differ in Brain-wide Connectivity and Function. Neuron *88*, 1253–1267.

Kinnischtzke, A.K., Sewall, A.M., Berkepile, J.M., and Fanselow, E.E. (2012). Postnatal maturation of somatostatin-expressing inhibitory cells in the somatosensory cortex of GIN mice. Front. Neural Circuits *6*, 33.

Koelbl, C., Helmstaedter, M., L'bke, J., and Feldmeyer, D. (2015). A barrel-related interneuron in layer 4 of rat somatosensory cortex with a high intrabarrel connectivity. Cereb. Cortex *25*, 713–725.

Kumar, P., and Ohana, O. (2008). Inter- and intralaminar subcircuits of excitatory and inhibitory

neurons in layer 6a of the rat barrel cortex. J. Neurophysiol. *100*, 1909–1922.

Kvitsiani, D., Ranade, S., Hangya, B., Taniguchi, H., Huang, J.Z., and Kepecs, a (2013). Distinct behavioural and network correlates of two interneuron types in prefrontal cortex. Nature *498*, 363–366.

Lee, S., Kruglikov, I., Huang, Z.J., Fishell, G., and Rudy, B. (2013). A disinhibitory circuit mediates motor integration in the somatosensory cortex. Nat. Neurosci. *16*, 1662–1670.

Lee, S.-H., Kwan, A.C., Zhang, S., Phoumthipphavong, V., Flannery, J.G., Masmanidis, S.C., Taniguchi, H., Huang, Z.J., Zhang, F., Boyden, E.S., et al. (2012). Activation of specific interneurons improves V1 feature selectivity and visual perception. Nature *488*, 379–383.

Levy, R.B., and Reyes, A.D. (2012). Spatial profile of excitatory and inhibitory synaptic connectivity in mouse primary auditory cortex. J. Neurosci. *32*, 5609–5619.

Litwin-Kumar, A., Rosenbaum, R., and Doiron, B. (2016). Inhibitory stabilization and visual coding in cortical circuits with multiple interneuron subtypes. J. Neurophysiol. jn.00732.2015.

Lorente de No, R. (1992). The Cerebral Cortex of the Mouse. Somat. Mot. Res. *9*, 3–36.

Ma, W., Liu, B., Li, Y., Huang, Z.J., Zhang, L.I., and Tao, H.W. (2010). Visual representations by cortical somatostatin inhibitory neurons--selective but with weak and delayed responses. J. Neurosci. *30*, 14371–14379.

Ma, Y., Hu, H., Berrebi, A.S., Mathers, P.H., and Agmon, A. (2006). Distinct subtypes of somatostatin-containing neocortical interneurons revealed in transgenic mice. J. Neurosci. *26*, 5069–5082.

Ma, Y., Hu, H., and Agmon, a. (2012). Short-Term Plasticity of Unitary Inhibitory-to-Inhibitory Synapses Depends on the Presynaptic Interneuron Subtype. J. Neurosci. *32*, 983–988.

Makino, H., and Komiyama, T. (2015). Learning enhances the relative impact of top-down processing in the visual cortex. Nat Neurosci *18*, 1116–1122.

Markram, H., Toledo-Rodriguez, M., Wang, Y., Gupta, A., Silberberg, G., and Wu, C. (2004). Interneurons of the neocortical inhibitory system. Nat. Rev. Neurosci. *5*, 793–807.

Marques-Smith, A., Lyngholm, D., Kaufmann, A.K., Stacey, J.A., Hoerder-Suabedissen, A., Becker, E.B.E., Wilson, M.C., Molnár, Z., and Butt, S.J.B. (2016). A Transient Translaminar GABAergic Interneuron Circuit Connects Thalamocortical Recipient Layers in Neonatal Somatosensory Cortex. Neuron *89*, 536–549.

Martinez, L.M., Wang, Q., Reid, R.C., Pillai, C., Alonso, J.M., Sommer, F.T., and Hirsch, J.A. (2005). Receptive field structure varies with layer in the primary visual cortex. Nat Neurosci *8*, 372–379.

McGarry, L.M., Packer, A.M., Fino, E., Nikolenko, V., Sippy, T., and Yuste, R. (2010). Quantitative

classification of somatostatin-positive neocortical interneurons identifies three interneuron subtypes. Front. Neural Circuits *4*, 12.

Merel, J., Shababo, B., Naka, A., Adesnik, H., and Paninski, L. (2016). Bayesian methods for event analysis of intracellular currents. J. Neurosci. Methods *269*, 21–32.

Miller, K.D. (2016). Canonical computations of cerebral cortex. Curr. Opin. Neurobiol. *37*, 75–84.

Morgenstern, N.A., Bourg, J., and Petreanu, L. (2016). Multilaminar networks of cortical neurons integrate common inputs from sensory thalamus. Nat. Neurosci. *19*, 1034–1040.

Muñoz, W., Tremblay, R., and Rudy, B. (2014). Channelrhodopsin-Assisted Patching: InVivo Recording of Genetically and Morphologically Identified Neurons throughout the Brain. Cell Rep. *9*, 2304–2316.

Muñoz, W., Tremblay, R., Levenstein, D., and Rudy, B. (2017). Layer-specific modulation of neocortical dendritic inhibition during active wakefulness. Science (80-.). *355*, 954 LP-959.

Murayama, M., Pérez-Garci, E., Nevian, T., Bock, T., Senn, W., and Larkum, M.E. (2009). Dendritic encoding of sensory stimuli controlled by deep cortical interneurons. Nature *457*, 1137–1141.

Nakajima, M., Görlich, A., and Heintz, N. (2014). Oxytocin modulates female sociosexual behavior through a specific class of prefrontal cortical interneurons. Cell *159*, 295–305.

Oliva, a a, Jiang, M., Lam, T., Smith, K.L., and Swann, J.W. (2000). Novel hippocampal interneuronal subtypes identified using transgenic mice that express green fluorescent protein in GABAergic interneurons. J. Neurosci. *20*, 3354–3368.

Otsuka, T., and Kawaguchi, Y. (2009). Cortical inhibitory cell types differentially form intralaminar and interlaminar subnetworks with excitatory neurons. J. Neurosci. *29*, 10533–10540.

Packer, A.M., and Yuste, R. (2011). Dense, unspecific connectivity of neocortical parvalbumin-positive interneurons: a canonical microcircuit for inhibition? J. Neurosci. *31*, 13260–13271.

Packer, A.M., McConnell, D.J., Fino, E., and Yuste, R. (2012). Axo-Dendritic Overlap and Laminar Projection Can Explain Interneuron Connectivity to Pyramidal Cells. Cereb. Cortex *23*, 2790–2802.

Pakan, J.M.P., Lowe, S.C., Dylda, E., Keemink, S.W., Currie, S.P., Coutts, C.A., and Rochefort, N.L. (2016). Behavioral-state modulation of inhibition is context-dependent and cell type specific in mouse visual cortex. Elife *5*, 1–18.

Petersen, C.C.H., and Sakmann, B. (2000). The excitatory neuronal network of rat layer 4 barrel cortex. J. Neurosci. *20*, 7579–7586.

Petreanu, L., Gutnisky, D. a., Huber, D., Xu, N., O'Connor, D.H., Tian, L., Looger, L., and Svoboda, K. (2012). Activity in motor–sensory projections reveals distributed coding in somatosensation. Nature 0–7.

Pfeffer, C.K., Xue, M., He, M., Huang, Z.J., and Scanziani, M. (2013). Inhibition of inhibition in visual cortex: the logic of connections between molecularly distinct interneurons. Nat. Neurosci. *16*, 1068–1076.

Pi, H.-J., Hangya, B., Kvitsiani, D., Sanders, J.I., Huang, Z.J., and Kepecs, A. (2013). Cortical interneurons that specialize in disinhibitory control. Nature *503*, 521–524.

Pluta, S., Naka, A., Veit, J., Telian, G., Yao, L., Hakim, R., Taylor, D., and Adesnik, H. (2015). A direct translaminar inhibitory circuit tunes cortical output. Nat. Neurosci. *advance on*.

Polack, P.-O., and Contreras, D. (2012). Long-range parallel processing and local recurrent activity in the visual cortex of the mouse. J. Neurosci. *32*, 11120–11131.

Poo, C., and Isaacson, J.S. (2009). Odor Representations in Olfactory Cortex: "Sparse" Coding, Global Inhibition, and Oscillations. Neuron *62*, 850–861.

Porter, J.T., Johnson, C.K., and Agmon, A. (2001). Diverse types of interneurons generate thalamus-evoked feedforward inhibition in the mouse barrel cortex. J. Neurosci. *21*, 2699–2710.

Pouille, F., Marin-Burgin, A., Adesnik, H., Atallah, B. V, and Scanziani, M. (2009a). Input normalization by global feedforward inhibition expands cortical dynamic range. Nat. Neurosci. *12*, 1577–1585.

Pouille, F., Marin-Burgin, A., Adesnik, H., Atallah, B. V, and Scanziani, M. (2009b). Input normalization by global feedforward inhibition expands cortical dynamic range. Nat. Neurosci. *12*, 1577–1585.

Reimer, J., Froudarakis, E., Cadwell, C.R., Yatsenko, D., Denfield, G.H., and Tolias, A.S. (2014). Pupil Fluctuations Track Fast Switching of Cortical States during Quiet Wakefulness. Neuron *84*, 355–362.

Rudy, B., Fishell, G., Lee, S., and Hjerling-Leffler, J. (2011). Three groups of interneurons account for nearly 100% of neocortical GABAergic neurons. Dev. Neurobiol. *71*, 45–61.

Salinas, E., and Thier, P. (2000). Gain Modulation : A Major Computational Principle of the Central Nervous System. Neuron *27*, 15–21.

Scholl, B., Pattadkal, J.J., Dilly, G.A., Priebe, N.J., and Zemelman, B. V. (2015). Local Integration Accounts for Weak Selectivity of Mouse Neocortical Parvalbumin Interneurons. Neuron *87*, 424–437.

Schubert, D., Staiger, J.F., Cho, N., Kötter, R., Zilles, K., and Luhmann, H.J. (2001). Layer-specific intracolumnar and transcolumnar functional connectivity of layer V pyramidal cells in rat barrel

cortex. J. Neurosci. *21*, 3580–3592.

Sekerli, M., Del Negro, C.A., Lee, R.H., and Butera, R.J. (2004). Estimating action potential thresholds from neuronal time-series: New metrics and evaluation of methodologies. IEEE Trans. Biomed. Eng. *51*, 1665–1672.

Seybold, B.A., Phillips, E.A.K., Schreiner, C.E., and Hasenstaub, A.R. (2015). Inhibitory Actions Unified by Network Integration. Neuron *87*, 1181–1192.

Shepherd, G.M.G., and Svoboda, K. (2005). Laminar and columnar organization of ascending excitatory projections to layer 2/3 pyramidal neurons in rat barrel cortex. J. Neurosci. *25*, 5670–5679.

Silberberg, G., and Markram, H. (2007). Disynaptic inhibition between neocortical pyramidal cells mediated by Martinotti cells. Neuron *53*, 735–746.

Tan, Z., Hu, H., Huang, Z.J., and Agmon, A. (2008). Robust but delayed thalamocortical activation of dendritic-targeting inhibitory interneurons. Proc. Natl. Acad. Sci. U. S. A. *105*, 2187–2192.

Tang, J.C.Y., Rudolph, S., Dhande, O.S., Abraira, V.E., Choi, S., Lapan, S.W., Drew, I.R., Drokhlyansky, E., Huberman, A.D., Regehr, W.G., et al. (2015). Cell type–specific manipulation with GFP-dependent Cre recombinase. Nat. Neurosci. *18*, 1334–1341.

Taniguchi, H., He, M., Wu, P., Kim, S., Paik, R., Sugino, K., Kvitsani, D., Fu, Y., Lu, J., Lin, Y., et al. (2011). A Resource of Cre Driver Lines for Genetic Targeting of GABAergic Neurons in Cerebral Cortex. Neuron *71*, 995–1013.

Tasic, B., Menon, V., Nguyen, T.N.T., Kim, T.T.K., Jarsky, T., Yao, Z., Levi, B.B., Gray, L.T., Sorensen, S.A., Dolbeare, T., et al. (2016). Adult mouse cortical cell taxonomy revealed by single cell transcriptomics. Nat. Neurosci. *advance on*, 1–37.

Tremblay, R., Lee, S., and Rudy, B. (2016). GABAergic Interneurons in the Neocortex: From Cellular Properties to Circuits. Neuron *91*, 260–292.

Tuncdemir, S.N., Wamsley, B., Stam, F.J., Osakada, F., Goulding, M., Callaway, E.M., Rudy, B., and Fishell, G. (2016). Early Somatostatin Interneuron Connectivity Mediates the Maturation of Deep Layer Cortical Circuits. Neuron *89*, 521–535.

Urban-Ciecko, J., and Barth, A.L. (2016). Somatostatin-expressing neurons in cortical networks. Nat. Rev. Neurosci. *17*, 401–409.

Wang, Y., Toledo-Rodriguez, M., Gupta, A., Wu, C., Silberberg, G., Luo, J., and Markram, H. (2004). Anatomical, physiological and molecular properties of Martinotti cells in the somatosensory cortex of the juvenile rat. J. Physiol. *561*, 65–90.

Williams, S.R., and Mitchell, S.J. (2008). Direct measurement of somatic voltage clamp errors in central neurons. Nat. Neurosci. *11*, 790–798.

Wilson, N.R., Runyan, C. a., Wang, F.L., and Sur, M. (2012). Division and subtraction by distinct cortical inhibitory networks in vivo. Nature *488*, 1–6.

Wimmer, V.C., Bruno, R.M., de Kock, C.P.J., Kuner, T., and Sakmann, B. (2010). Dimensions of a Projection Column and Architecture of VPM and POm Axons in Rat Vibrissal Cortex. Cereb. Cortex *20*, 2265–2276.

Wu, C., Ivanova, E., Zhang, Y., and Pan, Z.H. (2013). rAAV-Mediated Subcellular Targeting of Optogenetic Tools in Retinal Ganglion Cells In Vivo. PLoS One *8*, 1–10.

Xiang, Z., Huguenard, J.R., and Prince, D. a (1998). Cholinergic Switching Within Neocortical Inhibitory Networks. Science (80-.). *281*, 985–988.

Xu, X., and Callaway, E.M. (2009). Laminar specificity of functional input to distinct types of inhibitory cortical neurons. J. Neurosci. *29*, 70–85.

Xu, H., Jeong, H.Y., Tremblay, R., and Rudy, B. (2013). Neocortical Somatostatin-Expressing GABAergic Interneurons Disinhibit the Thalamorecipient Layer 4. Neuron *77*, 155–167.

Yavorska, I., and Wehr, M. (2016). Somatostatin-Expressing Inhibitory Interneurons in Cortical Circuits. Front. Neural Circuits *10*, 1–18.

Yoshimura, Y., and Callaway, E.M. (2005). Fine-scale specificity of cortical networks depends on inhibitory cell type and connectivity. Nat. Neurosci. *8*, 1552–1559.

Yoshimura, Y., Dantzker, J., and Callaway, E. (2005). Excitatory cortical neurons form fine-scale functional networks. Nature *433*.